The Astrophysical Journal, 932:68 (19pp), 2022 June 10 https://doi.org/10.3847/1538-4357/ac6d64
© 2022. The Author(s). Published by the American Astronomical Society.
OPEN ACCESS

Radial Trapping of Thermal Rossby Waves within the Convection Zones of Low-mass Stars

Bradley W. Hindman[1,2] and Rekha Jain[3]
[1] JILA, University of Colorado, Boulder, CO 80309-0440, USA; hindman@solarz.colorado.edu
[2] Department of Applied Mathematics, University of Colorado, Boulder, CO 80309-0526, USA
[3] School of Mathematics & Statistics, University of Sheffield, Sheffield S3 7RH, UK
Received 2022 March 8; revised 2022 April 20; accepted 2022 April 25; published 2022 June 16

Abstract

We explore how thermal Rossby waves propagate within the gravitationally stratified atmosphere of a low-mass star with an outer convective envelope. Under the conditions of slow, rotationally constrained dynamics, we derive a local dispersion relation for atmospheric waves in a fully compressible stratified fluid. This dispersion relation describes the zonal and radial propagation of acoustic waves and gravito-inertial waves. Thermal Rossby waves are just one class of prograde-propagating gravito-inertial wave that manifests when the buoyancy frequency is small compared to the rotation rate of the star. From this dispersion relation, we identify the radii at which waves naturally reflect and demonstrate how thermal Rossby waves can be trapped radially in a waveguide that permits free propagation in the longitudinal direction. We explore this trapping further by presenting analytic solutions for thermal Rossby waves within an isentropically stratified atmosphere that models a zone of efficient convective heat transport. We find that, within such an atmosphere, waves of short zonal wavelength have a wave cavity that is radially thin and confined within the outer reaches of the convection zone near the star's equator. The same behavior is evinced by the thermal Rossby waves that appear at convective onset in numerical simulations of convection within rotating spheres. Finally, we suggest that stable thermal Rossby waves could exist in the lower portion of the Sun's convection zone, despite that region's unstable stratification. For long wavelengths, the Sun's rotation rate is sufficiently rapid to stabilize convective motions, and the resulting overstable convective modes are identical to thermal Rossby waves.

Unified Astronomy Thesaurus concepts: Stellar convective zones (301); Stellar oscillations (1617); Solar oscillations (1515); Stellar rotation (1629); Solar rotation (1524); Internal waves (819); Hydrodynamics (1963); Asteroseismology (73); Helioseismology (709); Solar convective zone (1998); Polytropes (1281)

1. Introduction

The unambiguous detection of Rossby waves in the Sun by Löptien et al. (2018) has led to a flurry of observational efforts to characterize the waves and to search for other classes of inertial oscillations (e.g., Alshehhi et al. 2019; Hanasoge & Mandal 2019; Liang et al. 2019; Hanson et al. 2020; Proxauf et al. 2020; Gizon et al. 2021; Hathaway & Upton 2021; Mandal et al. 2021). As a result, there has been a resurrection of interest in inertial waves as they might apply to the Sun and solar-like stars (e.g., Lanza et al. 2019; Damiani et al. 2020; Gizon et al. 2020; Cai et al. 2021; Bekki et al. 2022). In particular, Gizon et al. (2021) have raised the intriguing possibility that inertial oscillations might be a sensitive seismic diagnostic for the properties of the deep convection zone, such as the radial profiles of the superadiabatic gradient and the turbulent viscosity. For a recent review of inertial oscillations in the solar context, see the review by Zaqarashvili et al. (2021).

There is a menagerie of inertial oscillations that might exist within a star (e.g., Bryan 1889; Greenspan 1968; Rieutord 1991; Lindblom & Ipser 1999; Lockitch & Friedman 1999). However, the classical Rossby waves—coined r modes in astrophysics (Papaloizou & Pringle 1978a)—have received the bulk of the attention of the stellar physics community (e.g., Provost et al. 1981; Saio 1982; Wolff & Blizard 1986; Lee & Saio 1987; Lee et al. 1992; Saio et al. 2018; Van Reeth et al. 2018; Li et al. 2019). The r modes are primarily two-dimensional (2D) vorticity waves, with incompressive horizontal motions confined largely to spherical surfaces. As such motions do not generate pressure or buoyancy fluctuations, the Coriolis force is the only active restoring force.

Classical Rossby waves conserve the radial component of their absolute vorticity. If $\boldsymbol{\Omega}$ is the rotation vector of the star and the flow velocity in the rotating frame of reference is $\boldsymbol{u}$, then the relative vorticity of the flow is $\boldsymbol{\omega} = \boldsymbol{\nabla} \times \boldsymbol{u}$ and the "planetary" vorticity is $2\boldsymbol{\Omega}$. The absolute vorticity is their sum, $\boldsymbol{\omega}_a = \boldsymbol{\omega} + 2\boldsymbol{\Omega}$, and the conservation principle can be written:

$$\frac{D}{Dt}(\boldsymbol{\omega}_a \cdot \hat{\boldsymbol{r}}) = \frac{D}{Dt}(\omega_r + 2\Omega_r) = 0, \tag{1}$$

where ω_r and $\Omega_r = \Omega \cos\theta$ are the radial components of the relative vorticity and the rotation vector, respectively. The angle θ is the colatitude and $\hat{\boldsymbol{r}}$ is the radial unit vector of the spherical coordinate system whose axis is aligned with the rotation vector.

In the northern hemisphere, as a spinning parcel of fluid is pushed northward, the radial component of the planetary vorticity $2\Omega_r$ increases and there must be a corresponding decrease in the relative vorticity ω_r. A parcel pushed equatorward has the converse effect; the radial component of the planetary vorticity is reduced and the relative vorticity must increase to compensate. For the poleward-pushed parcel, the

Original content from this work may be used under the terms of the Creative Commons Attribution 4.0 licence. Any further distribution of this work must maintain attribution to the author(s) and the title of the work, journal citation and DOI.

decrease in relative vorticity is consistent with adding an anticyclonic vortex to the fluid parcel, and through vortex–vortex interactions this new clockwise motion will push all nearby fluid elements. Fluid located to the east is pushed poleward, and fluid to the west is pushed equatorward. These pushed fluid elements will conserve their own absolute vorticity and in turn push fluid elements that are further and further away. One can see that the net result is a north–south undulation that travels to the west, or equivalently in the retrograde direction. In the preceding discussion, we are using the words east and west in terms of the directions on the stellar globe, *not* in terms of the directions on the plane of the sky (as is often done by solar astronomers).

There is another class of Rossby wave, called the thermal Rossby wave (i.e., Roberts 1968; Busse 1970), that operates on a similar principle of conservation of potential vorticity. The motions in a thermal Rossby wave are also 2D, but instead of motion on spherical surfaces, the thermal Rossby wave has motions that are perpendicular to the rotation axis. Specifically, the motion generally manifests as a belt of nearly geostrophic Taylor columns that gird the equator, and except for where they intersect with the star's spherical surface, are largely invariant in the direction of the rotation vector—see the review by Busse (2002). Every other column in the belt has right-handed spin, and columns with left-handed spin are interleaved between. A full longitudinal wavelength is hence two counterspinning columns.

Each spinning Taylor column conserves angular momentum locally, and when expressed as a potential vorticity, the conservation law takes on the form (Gibbons 1980; Glatzmaier & Gilman 1981; Unno et al. 1989)

$$\frac{D}{Dt}\left(\frac{\boldsymbol{\omega}_a \cdot \hat{\boldsymbol{\Omega}}}{\rho L}\right) = \frac{D}{Dt}\left(\frac{\omega_y + 2\Omega}{\rho L}\right) = 0, \tag{2}$$

where $\omega_y = \boldsymbol{\omega} \cdot \hat{\boldsymbol{\Omega}}$ is the component of the relative vorticity aligned with the rotation axis, ρ is the mass density, and L is the height of the Taylor column, i.e., the length of the chord that runs along the column's axis from the stellar surface in the southern hemisphere to the same spherical surface in the north —see Figure 1 of Glatzmaier & Gilman (1981).

If a spinning column near the equator is pushed toward the rotation axis, the column grows in height (L increases) as the chord length of the column's axis increases. In an incompressible fluid, this vortex stretching is accompanied by a commensurate narrowing of the column to conserve mass. Subsequently, as the column compresses laterally, the column must spin faster to conserve angular momentum about its own axis (e.g., Hide 1966; Busse 1970). In Equation (2), this conservation principle is enforced by the constancy of the potential vorticity, $(\omega_y + 2\Omega)/\rho L$. As L increases, ω_y must also increase. The resulting induced vorticity causes the neighboring column to the west to be pushed outward, away from the rotation axis, and the column to the east to be pushed inward, toward the rotation axis. These newly pushed columns conserve their own potential vorticity (i.e., angular momentum) and induce spinning columns further down the belt to also move inward and outward. The result is a prograde-propagating Rossby wave where the spinning columns dance back and forth, toward and away from the rotation axis. This type of wave has received significant attention in the geophysics community, as *thermal* convection in a rotating spherical shell of fluid appears at onset as an unstable *thermal* Rossby wave (e.g., Roberts 1968; Busse 1970; Dormy et al. 2004; Jones et al. 2009; Kaplan et al. 2017).

In a compressible fluid, an additional mechanism comes into play (Gibbons 1980; Glatzmaier & Gilman 1981; Ando 1989). In complement to the topological effect of the changing column height as the column moves inward or outward, gravitational stratification leads to a change in the mass density of the column as the column is pushed into a region with different pressure. If the column is pushed closer to the rotation axis, the increase in pressure leads to an increase in density, and conservation of mass and angular momentum dictate that the column must narrow and consequently spin faster cyclonically. This stratification effect is embodied by the factor of density that appears in the denominator of the potential vorticity in Equation (2).

The topological and stratification effects act in concert to enhance spin as a column is moved inward, and hence they both lead to prograde wave propagation. The topological effect, sometimes called the topological β-effect, is the dominant effect in the molten interiors of rocky planets, as the density contrast as a function of radius is rather modest and one can safely assume that the fluid is incompressible. In stars, however, many density scale heights fit within the stellar radius, and as a result, the topological effect is usually ancillary to the stratification. For instance, Glatzmaier & Gilman (1981) argue that the stratification effect dominates if a star spans more than one density scale height (the Sun's convection zone spans roughly 11 scale heights).

To our knowledge, thermal Rossby waves have not yet been observed in the Sun or identified asteroseismically in other stars. However, they are a conspicuous feature in laboratory experiments of convection in a rotating fluid (e.g., Mason 1975; Busse & Hood 1982; Azouni et al. 1985; Chamberlain & Carrigan 1986; Sommeria et al. 1991; Cordero & Busse 1992; Smith et al. 2014). In fact, thermal Rossby waves are often used as a proxy for understanding classical Rossby waves, by building a spinning tank of fluid with sloping upper or lower boundaries, thus allowing one to control the sign and magnitude of the topological β-effect. Further, in numerical simulations of stellar convection in spherical geometry, nonlinear thermal Rossby waves play a crucial role in the transport of angular momentum and heat throughout the star's convection zone. In particular, they are essential for generating differential rotation by redistributing angular momentum. These waves appear prominently at convective onset, when the Rayleigh number just exceeds the critical value required for convective overturning. The first convective instability to appear is a buoyantly driven thermal Rossby wave that manifests at low latitudes just below the outer surface. In terms of spherical harmonics, this wave is composed of a single unstable azimuthal order m and a small range of harmonic degrees corresponding to equatorially trapped harmonics, $\ell \approx m$. The wave is unstable, but its amplitude saturates at a low amplitude due to nonlinear effects. Figure 1 illustrates the type of thermal Rossby wave that is seen in such simulations (i.e., Hindman et al. 2020a). Both panels show the axial component of the vorticity (i.e., the component that is parallel to the rotation vector, $\omega_y = \boldsymbol{\omega} \cdot \hat{\boldsymbol{\Omega}}$). The rotation axis is aligned with the coordinate axis, with north being upward in the image. The left-hand panel is an orthographic projection of the axial vorticity on a spherical surface with a radius that is just below

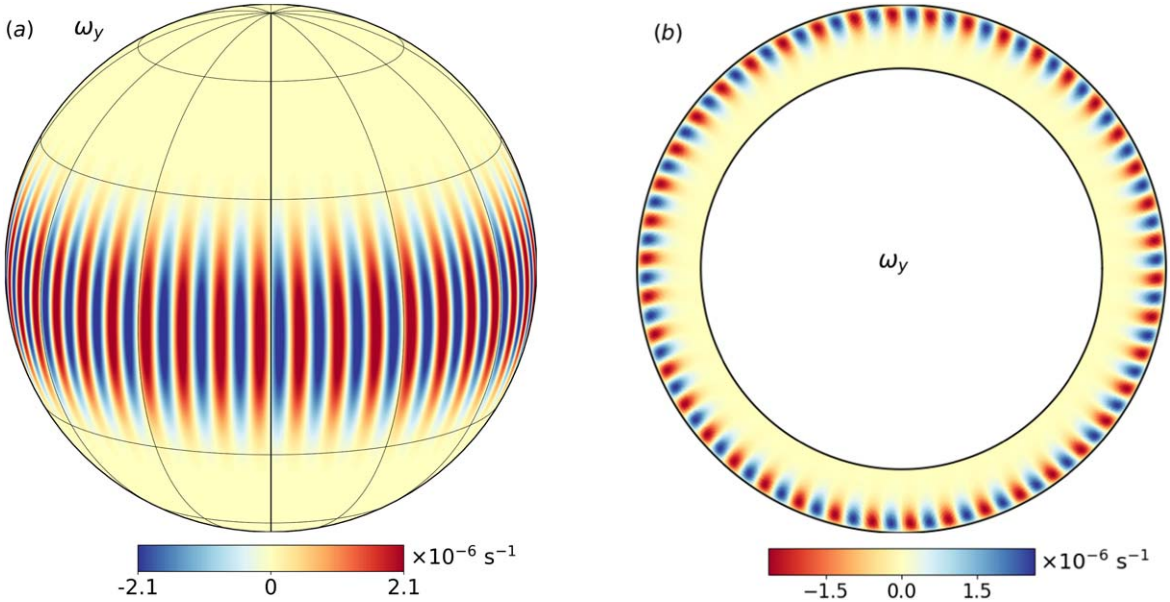

Figure 1. An example of a thermal Rossby wave that appears prominently at convective onset in a 3D numerical simulation of convection in a spherical shell, specifically Model #68 from Hindman et al. (2020a). (a) The axial vorticity ($\omega_y = \boldsymbol{\omega} \cdot \hat{\boldsymbol{\Omega}}$) in orthographic projection shown on a spherical surface that lies just below the outer boundary of the computation domain. Red tones indicate anticyclonic vortices and blue tones cyclonic flow. This particular simulation produces a wave with 42 complete wavelengths girding the equator ($m = 42$). Each zonal wavelength consists of two counterspinning rolls whose axes are aligned with the rotation vector. (b) The axial component of the vorticity illustrated on the equatorial plane as viewed from above the north pole. Red tones indicate anticyclonic (clockwise) vortices and blue tones correspond to those that are cyclonic (counterclockwise). From these images, it is clear that the thermal Rossby wave is trapped radially and latitudinally; the wave resides in a cavity that is confined to low latitudes and to radii that lie very close to the outer surface. The numerical simulations that generated the flow data illustrated by these images were generated by the Rayleigh convection code (Featherstone & Hindman 2016; Matsui et al. 2016; Featherstone et al. 2021).

the outer surface of the simulation domain. Red tones indicate anticyclonic vorticity and blue tones cyclonic. This particular simulation has 42 complete wavelengths that wrap around the equator ($m = 42$). The right-hand panel of Figure 1 portrays axial vorticity in the equatorial plane. It is clear that each zonal wavelength consists of two counterrotating vortices and that the wave is trapped in the upper reaches of the model's convection zone.

This concentration of the thermal Rossby wave's energy density in the outer portion of the star's convection zone is a direct consequence of the density stratification. In an incompressible fluid, the thermal Rossby waves that appear at convective onset are concentrated in the deepest portions of the shell. But with even a moderate degree of stratification—one or more density scale heights across the shell, the wave's energy density begins to shift and cling to the outer surface (e.g., Busse et al. 2005; Jones et al. 2009; Hindman et al. 2020a). The radial structure of a thermal Rossby wave's eigenfunction and the way in which the waves are reflected and trapped in a waveguide are still poorly understood when the fluid is stratified. Elucidating why these reflections occur and where the waveguide resides will be our goal here.

In helio- and asteroseismology, when exploring the properties of the waveguides that trap p modes and g modes, it is common practice to extract a local dispersion relation from the fluid equations and to discern the regions of a star where a wave with a particular frequency and horizontal wavenumber is radially propagating and where it is evanescent (e.g., Unno et al. 1989; Gough 1993; Christensen-Dalsgaard 2003). In this way, the radial extent of the waveguide can be identified as the zone of propagation without ever needing to completely solve for the mode eigenfunctions. We will apply this standard technique here to define the radial boundaries of the waveguide for thermal Rossby waves and to characterize which properties of the star (e.g., the stratification and rotation rate) determine the location of those boundaries.

A local dispersion relation for thermal Rossby waves has been derived previously by Ando (1989) and subsequently simplified by Unno et al. (1989) for the special case of waves propagating perpendicular to the rotation vector through an isentropic stratification. If ω is the temporal frequency of the wave (not to be confused with the vorticity), k_x is the zonal wavenumber, k_z is the radial wavenumber, and H is the density scale height, Unno et al. (1989) obtain the following relation:

$$\omega = \frac{2\Omega k_x}{(k_x^2 + k_z^2)H}. \tag{3}$$

Both Ando (1989) and Unno et al. (1989) correctly comment that the wave propagates in the prograde direction, and as such, Unno et al. (1989) calls the thermal Rossby wave the "low-frequency prograde wave." As we will see, their expression is valid only in the extreme limit that the wavelength is drastically shorter than the local density scale height. Thus, in their derivation they have dropped a variety of terms that depend on the star's radial stratification. We will demonstrate that these dropped terms can cause reflection and thus enable radial trapping of the thermal Rossby wave.

In addition to deriving a more complete local dispersion relation that self-consistently accounts for the gravitational stratification, we will explore the nature of the resulting waveguide, or wave cavity, by presenting analytic solutions for the eigenfunctions and eigenfrequencies that apply when the atmosphere is isentropically stratified. Such stratification has been examined often in the past (e.g., Papaloizou & Pringle 1978b; Glatzmaier & Gilman 1981; Busse et al. 2005; Wu 2005; Busse & Simitev 2014; Ouazzani et al. 2020)

because in such an atmosphere the internal gravity waves and their coupling to the inertial waves are suppressed. With these eigenfunctions, we will demonstrate that when the thermal Rossby wave is a pure inertial wave (instead of a mixed gravito-inertial wave), the concentration of the thermal Rossby wave's energy density near the upper boundary of a stellar convection zone is a natural consequence for waves with a zonal wavelength that is much shorter than the depth of the convection zone.

In Section 2, we present the fluid equations for a completely compressible fluid and argue that the solutions are 2D when the wave motions are sufficiently slow and the frequency is low. From these equations, in Section 3, we derive a local dispersion relation for gravito-inertial waves that is valid for a completely general radial stratification. In Section 4, we specialize to an isentropically stratified atmosphere and present analytic solutions for the resulting inertial waves. Finally, in Section 5, we discuss the implications of our results for the Sun and other low-mass stars.

2. Atmospheric Waves in a Rotating Star

Our ultimate goal is to generate a simple, easily interpreted local dispersion relation for thermal Rossby waves that is applicable in a gravitationally stratified atmosphere. From this dispersion relation, we will deduce where waves reflect in the atmosphere and thus map the radial extent of the waveguide or cavity in which the thermal Rossby waves are trapped. In this section, we will derive the governing wave equation that applies in a simplified geometry.

We will be implicitly thinking about how the waves propagate and reflect within a low-mass star that possesses an outer convection zone, but many of the ideas that we develop will apply to more massive stars as well. In a general stratification, atmospheric waves come in many forms: acoustic waves, internal gravity waves, surface gravity waves, inertial waves, and all of their potential hybrids. In a star, the acoustic waves, or p modes, generally appear at high frequency, and thus their behavior can often be separated from that of the coupled, low-frequency, gravito-inertial waves. Thermal Rossby waves are but one type of the general class of gravito-inertial waves.

2.1. 2D Rotationally Constrained Flow in a Local Cartesian Domain

In regions of a star that are stably stratified, vertical movement is strongly inhibited and motions are often assumed to be horizontal and confined to spherical surfaces. When deriving the r modes of a star, this assumption is called the traditional approximation of rotation. In regions with an unstable or neutrally stable stratification, vertical motion is no longer restricted and the traditional approximation is not appropriate for all inertial waves. Instead, we start by assuming that the motions are rotationally constrained (i.e., slow compared to the rotational speeds) and hence the Taylor–Proudman theorem applies. This theorem dictates that slow motions are invariant in the direction of the rotation vector $\mathbf{\Omega}$, and therefore we can treat the problem as 2D. This 2D approximation is a standard one (Busse 1970, 2002; Glatzmaier & Gilman 1981; Busse et al. 2005; Busse & Simitev 2014), but of course, in a star with spherical geometry, there are many reasons that the Taylor–Proudman theorem breaks down on global spatial scales. Even so, the Coriolis force leads to a strong tendency toward 2D motion, and the Taylor–Proudman theorem can still hold locally over surprisingly long length scales. In our work here, we will ignore these potential 3D effects, because the full spherical geometry begets complicated mathematics and thus hinders qualitative understanding.

Numerical simulations (e.g., Hindman et al. 2020a) and linear stability analyses (Soward & Jones 1983; Yano 1992; Jones et al. 2009) demonstrate that the thermal Rossby waves that appear at convective onset in a gravitationally stratified spherical shell have the properties that the waves propagate in the longitudinal direction and are essentially 2D in nature. The waves appear as a parade of convective rolls that wrap around the equator. The axis of each roll is aligned with the rotation vector, and the roll is largely invariant along its own axis except where the axis intersects with the outer spherical surface. Whenever the zonal wavelength is much smaller than the outer radius of the convection zone, the waves are confined within a radially thin cavity that hugs the outer surface of the convection zone near the equator. Further, since the waves are essentially 2D in nature, the waves are equatorially as well as radially trapped. For example, the bottom of the wave cavity at the equator can be projected along a cylindrical surface whose axis is perpendicular to the equatorial plane. Hence, the cavity is confined in cylindrical radius instead of spherical radius and modes with a deep cavity (at the equator) extend further north and south of the equator. Figure 1 illustrates these properties by presenting a thermal Rossby wave as it appears in the 3D numerical simulation of Hindman et al. (2020a). Other examples can be viewed and downloaded at Hindman et al. (2020b). The numerically computed eigenfunctions obtained by Bekki et al. (2022) in spherical geometry also illustrate the cylindrical nature of the lower boundary of the wave cavity.

We will exploit these properties and make a short longitudinal wavelength approximation. Thus, over the shallow layer within which the wave resides, we can ignore the radial variation in the gravitational acceleration. Further, we can ignore the curvature of the isopycnals. These assumptions allow us to treat the background fluid as a plane-parallel atmosphere with constant gravity. This is similar to the approximation that is often made for the p modes in helioseismology (e.g., Lamb 1945; Gough 1993; Hindman & Zweibel 1994); for large harmonic degrees (i.e., large horizontal wavenumbers), the acoustic waves are trapped in a thin planar waveguide that lies just below the photosphere.

We will solve the fluid equations in a local Cartesian coordinate system whose origin is located at the equator on the star's outer surface. We align the unit vectors, $\hat{\boldsymbol{x}}$, $\hat{\boldsymbol{y}}$, and $\hat{\boldsymbol{z}}$, of this coordinate system such that $\hat{\boldsymbol{x}}$ points in the longitudinal direction, $\hat{\boldsymbol{y}}$ points in the latitudinal direction (parallel to the rotation vector, $\mathbf{\Omega} = \Omega\hat{\boldsymbol{y}}$), and $\hat{\boldsymbol{z}}$ is aligned with the radial direction (or antialigned with gravity, $\boldsymbol{g} = -g\hat{\boldsymbol{z}}$). If r, θ, and ϕ are the radius, colatitude, and longitude of a spherical coordinate system whose axis is aligned with the rotation vector, the three Cartesian coordinates can be mapped onto the spherical coordinates through $x = R\ \phi$, $y = R(\pi/2 - \theta)$, and $z = r - R$, where R is the radius of the stellar photosphere. We will interchangeably refer to z as the radial or vertical coordinate, and x and y as horizontal coordinates. This Cartesian coordinate system is similar to an f-plane model, except that the rotation vector points horizontally in the latitudinal direction. In a traditional f-plane model, the

horizontal component of the rotation vector is ignored and the *vertical* component is treated as constant. Here, we will instead ignore the vertical component and impose homogeneity of the *latitudinal* component.

2.2. Background Atmosphere for a General Stratification

As is typically done, we decompose all of the fluid variables into a steady background term and a temporally oscillating fluctuation, where the background is denoted with a "0" subscript and the Eulerian fluctuations with "1." Since the gravity in our plane-parallel atmosphere is purely vertical, all of the thermodynamic variables of the background are functions of z alone. Hence, the background pressure, mass density, and temperature are, respectively, $P_0(z)$, $\rho_0(z)$, and $T_0(z)$. These background thermodynamic profiles obey the hydrostatic condition and the ideal gas law,

$$\frac{dP_0}{dz} = -g\rho_0, \tag{4}$$

$$P_0 = \rho_0 R_{\rm gas} T_0, \tag{5}$$

where $R_{\rm gas}$ is the gas constant.

Since we will be considering gravito-inertial waves, the buoyancy frequency, N, will be an important atmospheric profile. The buoyancy frequency can be expressed in terms of the density scale height, H, and the sound speed, c:

$$N^2 = g\left(\frac{1}{H} - \frac{g}{c^2}\right), \tag{6}$$

$$H^{-1} \equiv -\frac{1}{\rho_0}\frac{d\rho_0}{dz}, \tag{7}$$

$$c^2 \equiv \gamma R_{\rm gas} T_0, \tag{8}$$

where γ is the gas's adiabatic exponent. Throughout Sections 2 and 3, we shall consider a general stratification where any reasonable functional form for the atmospheric profiles will be possible. Later, in Section 4, we will specialize to an isentropic atmosphere for which $N^2 = 0$.

2.3. Wave Equation for Atmospheric Waves

In our plane-parallel atmosphere, the 2D nature of the gravito-inertial waves manifests as invariance along the y axis and a lack of motion in that same direction. Thus, the fluid velocity $\boldsymbol{u}$ is purely lateral to the rotation vector $\boldsymbol{\Omega}$ and depends only on time and on the longitudinal and radial coordinates, x and z, respectively, $\boldsymbol{u} = u(x, z, t)\,\hat{\boldsymbol{x}} + w(x, z, t)\,\hat{\boldsymbol{z}}$. Further, if we ignore ionization and diffusive effects, the linearized fluid equations for an ideal gas take on the following form:

$$\frac{\partial \boldsymbol{u}}{\partial t} = 2\boldsymbol{u} \times \boldsymbol{\Omega} - \frac{1}{\rho_0}\boldsymbol{\nabla} P_1 + \boldsymbol{g}\frac{\rho_1}{\rho_0}, \tag{9}$$

$$\frac{\partial P_1}{\partial t} + w\frac{dP_0}{dz} = c^2\left(\frac{\partial \rho_1}{\partial t} + w\frac{d\rho_0}{dz}\right), \tag{10}$$

$$\frac{\partial \rho_1}{\partial t} = -\boldsymbol{\nabla}\cdot(\rho_0\boldsymbol{u}), \tag{11}$$

where we have adopted an adiabatic energy Equation (10) and a continuity Equation (11) that describes a completely compressible fluid. The quantities ρ_1 and P_1 are the Eulerian fluctuations of the mass density and gas pressure, respectively.

Since the background atmosphere is steady and longitudinally invariant, we will assume plane-wave solutions for the longitudinal and temporal variables. Therefore, all fluid variables will have the following form:

$$w \propto e^{ik_x x}\, e^{-i\omega t}, \tag{12}$$

with k_x being the longitudinal wavenumber and ω the temporal frequency. When a correspondence is drawn with spherical coordinates, the zonal wavenumber is directly proportional to the azimuthal order $m = k_x R$ of the associated spherical harmonic. Note that the sign convention we have adopted is such that waves with positive wavenumbers ($k_x > 0$) have prograde phase speeds for positive frequencies ($\omega > 0$) and retrograde phase speeds for negative frequencies ($\omega < 0$).

Our experience with acoustic-gravity waves suggests that a clean working variable is the reduced Lagrangian pressure fluctuation, $\delta\varpi$, which is related to the Eulerian pressure fluctuation through an additive advective term,

$$\delta\varpi \equiv \frac{P_1}{\rho_0} - \frac{\boldsymbol{u}\cdot\boldsymbol{\nabla}P_0}{i\omega\rho_0} = \frac{P_1}{\rho_0} + \frac{gw}{i\omega}. \tag{13}$$

By utilizing the definition of the buoyancy frequency (6), hydrostatic balance of the background state (4), and the continuity equation (11), we can rewrite the momentum and energy equations in terms of the two velocity components, u and w, and the reduced Lagrangian pressure fluctuation, $\delta\varpi$:

$$i\omega\,\delta\varpi = c^2\boldsymbol{\nabla}\cdot\boldsymbol{u} = c^2\left(ik_x u + \frac{dw}{dz}\right), \tag{14}$$

$$u = \frac{\sigma^2\omega}{\omega^4 - \sigma^4}\left[\frac{d}{dz} + \frac{\omega^2 k_x}{\sigma^2} - \frac{1}{H}\right]\delta\varpi, \tag{15}$$

$$w = -\frac{i\omega^3}{\omega^4 - \sigma^4}\left[\frac{d}{dz} + \frac{\sigma^2 k_x}{\omega^2} - \frac{1}{H}\right]\delta\varpi. \tag{16}$$

Equations (15) and (16) have been obtained from the two components of the momentum equation by using the definition of the Lagrangian pressure fluctuation (13), the modified energy equation (14), and the continuity equation (11) to eliminate the Eulerian pressure fluctuation P_1, the density fluctuation ρ_1, and the vertical derivative of the vertical velocity dw/dz. The resulting equations have then been cross-multiplied and subtracted to generate an equation that depends only on the horizontal velocity component u and another that depends only on the vertical velocity w.

For compactness in these expressions, we have defined a frequency, σ,

$$\sigma^2 \equiv gk_x - 2\Omega\omega, \tag{17}$$

that generates the dispersion relation $\omega^2 = \sigma^2$ for surface gravity waves, or f modes, in our rotating star. The existence of such a solution can be deduced from Equations (15) and (16) by seeking nontrivial solutions for the velocity components under the condition that the motions are incompressible ($\delta\varpi = 0$). Due to the orthogonality of gravity and the rotation vector at the equator, these solutions differ from the traditional Poincaré waves—see Section 5.5 for details.

Equations (14)–(16) can be combined to generate an ODE whose dependent variable is the reduced Lagrangian pressure

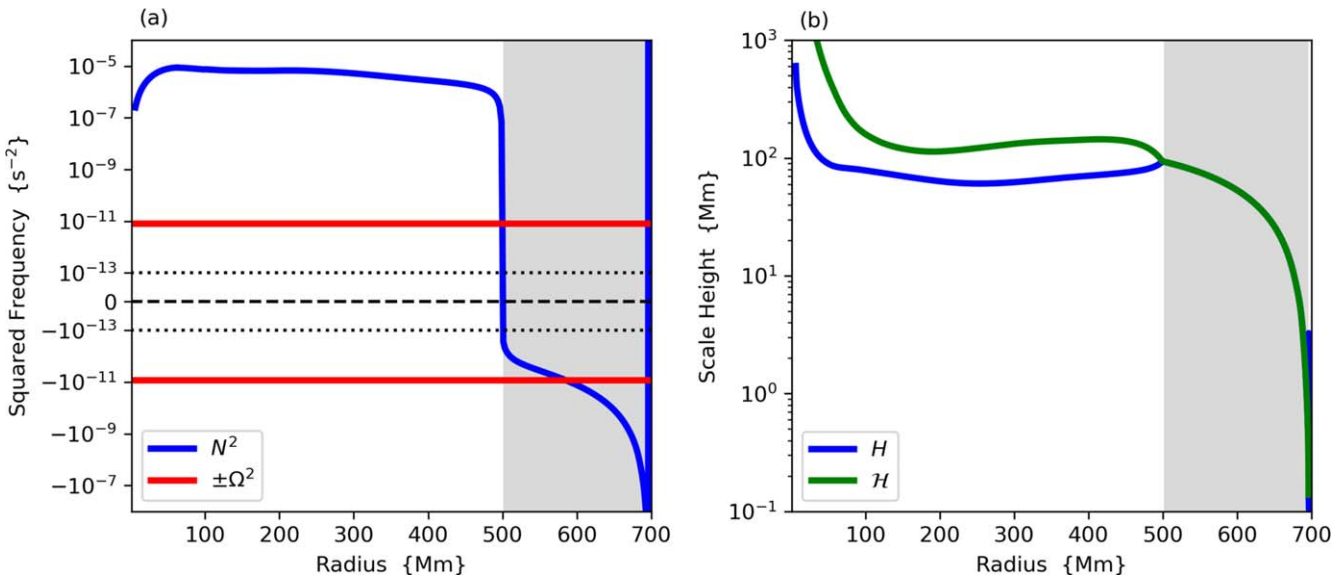

Figure 2. Radial atmospheric profiles for the Sun, as specified by Model S from Christensen-Dalsgaard et al. (1996). (a) The square of the buoyancy frequency N^2 is illustrated with the blue curve as a function of radius. The ordinate axis is logarithmically scaled in both the positive and negative values, with a region of linear scaling in the middle that extends between the dotted lines. The Sun's convection zone coincides with the region where the square of the buoyancy frequency is negative, and is indicated by the gray shaded region. The two red horizontal lines mark the square of the Carrington rotation rate, $\pm\Omega\odot^2$, where $\Omega = \Omega_\odot = 2.87 \times 10^{-6}$ s^{-1}. The entire radiative interior is in the regime of slow rotation, $N \gg \Omega$. (b) The density scale height H (blue curve) and the scale height $\mathcal{H}$ (green curve) shown as functions of radius in the Sun. The two scale heights are nearly identical in the convection zone and have roughly the same magnitude throughout much of the radiative interior.

fluctuation, $\delta\varpi$:

$$\left\{\frac{d^2}{dz^2} - \frac{1}{H}\frac{d}{dz} + \left[\frac{\omega^2 - 4\Omega^2}{c^2} + \frac{H'}{H^2} - k_x^2\left(1 - \frac{N^2}{\omega^2}\right) + \frac{2\Omega k_x}{\omega}\left(\frac{1}{H} - \frac{2N^2}{g}\right)\right]\right\}\delta\varpi = 0. \tag{18}$$

This governing equation is valid for a general stratification and for a completely compressible fluid. All of the atmospheric profiles are general functions of height, i.e., $H = H(z)$ and $N^2 = N^2(z)$. For compactness of notation, when convenient, we use a prime to indicate derivatives with respect to the vertical coordinate z. Hence, $H' = dH/dz$ is the vertical derivative of the density scale height.

3. Local Dispersion Relation for a General Stratification

The governing equation (18) can be rewritten in standard form (i.e., as a Helmholtz equation) by making a change of variable, $\delta\varpi(z) = \rho_0^{-1/2}\Psi(z)$, that has been explicitly chosen to ensure that the resulting ODE for $\Psi(z)$ lacks a first derivative term:

$$\frac{d^2\Psi}{dz^2} + k_z^2(z)\Psi(z) = 0, \tag{19}$$

$$k_z^2(z) \equiv \frac{\omega^2 - (\omega_c^2 + 4\Omega^2)}{c^2} - k_x^2\left(1 - \frac{N^2}{\omega^2}\right) + \frac{2\Omega k_x}{\omega\mathcal{H}}. \tag{20}$$

In the expression for k_z^2, the acoustic-cutoff frequency, ω_c, has the standard definition

$$\omega_c^2 \equiv \frac{1 - 2H'}{4H^2}\, c^2, \tag{21}$$

and $\mathcal{H}$ is a scale height that depends on the stratification,

$$\frac{1}{\mathcal{H}} \equiv \frac{1}{H} - \frac{2N^2}{g}. \tag{22}$$

In a stellar convection zone where $N^2 \approx 0$, the scale height $\mathcal{H}$ is nearly equal to the density scale height, but even in a region of stable stratification, $\mathcal{H}$ is positive and in low-mass stars has the same magnitude as the density scale height. Figure 2 illustrates the buoyancy frequency, the density scale height H, and the scale height $\mathcal{H}$ as predicted by an evolutionary model of the Sun's internal structure, i.e., Model S from Christensen-Dalsgaard et al. (1996).

The quantity $k_z(z)$ is a local radial wavenumber that varies with height in the atmosphere, and Equation (20) is a local dispersion relation that describes acoustic waves and gravito-inertial waves. This local dispersion relation reduces to the well-known expression for acoustic-gravity waves when the rotation rate vanishes. The inclusion of the Coriolis force provides two modifications. First, there is an effective correction to the acoustic-cutoff frequency (i.e., $\omega_c^2 \to \omega_c^2 + 4\Omega^2$) that is exceedingly weak in most stars. Second, the last term in Equation (20) is solely due to the Coriolis force, and it is responsible for generating inertial waves.

The local dispersion relation constitutes a fourth-order polynomial equation in ω, and hence for any given value of the vertical wavenumber, k_z, there are four solutions. Two of the solutions correspond to high-frequency acoustic waves and two to low-frequency gravito-inertial waves. In the limit of an isothermal atmosphere, all of the atmospheric profiles become constants—and hence the vertical wavenumber k_z is a constant. Figure 3 provides two propagation diagrams, which illustrate the frequencies for which the solutions are radially oscillatory in an isothermal atmosphere. The two panels correspond to different values of the ratio of the rotation rate and the buoyancy frequency. The shaded regions indicate the domains

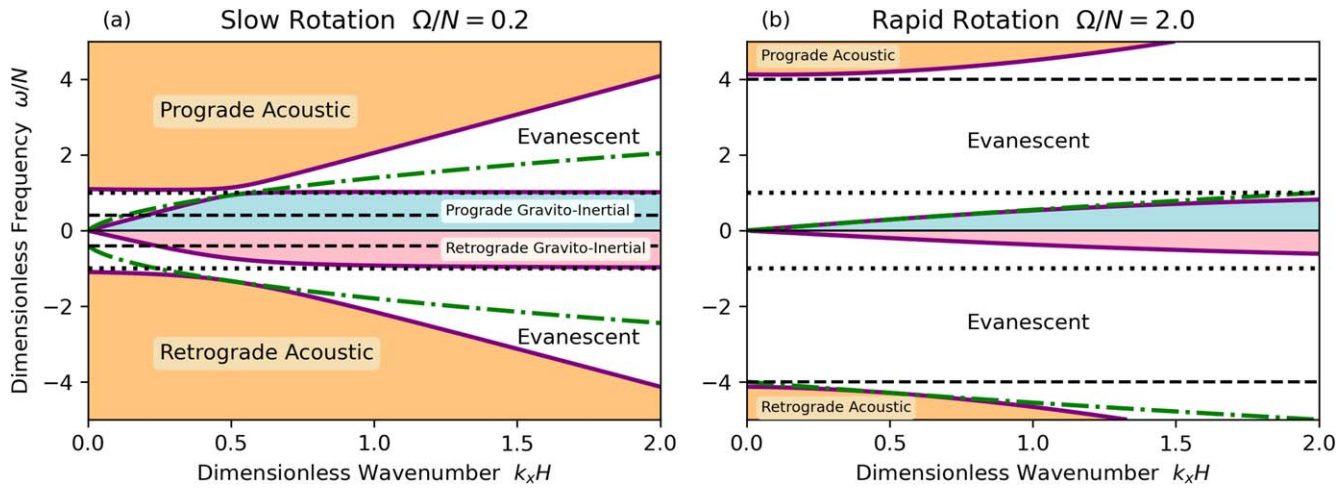

Figure 3. Propagation diagrams for an isothermal atmosphere in the limits of (a) slow rotation and (b) rapid rotation. For each limit, the ratio of the buoyancy frequency to the rotation rate is indicated at the top of the panel. Those frequencies and wavenumbers that correspond to radially propagating waves appear in the shaded regions. The prograde and retrograde branches of the acoustic waves appear in orange. The light blue region indicates gravito-inertial waves that propagate zonally in the prograde direction, and the pink region contains the retrograde gravito-inertial waves. The horizontal lines indicate the characteristic frequencies of the atmosphere. The dotted lines mark the positive and negative values of the buoyancy frequency, $\omega = \pm N$, and the dashed lines bound the inertial frequency range, $\omega = \pm 2\Omega$. At low wavenumbers, the low-frequency waves are gravito-inertial waves that have distinctly anisotropic branches. At high wavenumbers, these waves become nearly isotropic internal gravity waves. The two dotted–dashed green curves indicate the f modes for the rotating star.

of vertical propagation where the wavenumber k_z is real-valued ($k_z^2 > 0$). The white, unshaded regions correspond to evanescent waves, where the wavenumber k_z is purely imaginary ($k_z^2 < 0$) and the solutions are exponentially growing or decaying with height. The high-frequency acoustic waves fall into the orange portions of the diagram, with disjoint prograde and retrograde solution branches. For an atmosphere with convectively stable stratification ($N^2 > 0$), such as an isothermal atmosphere, the low-frequency gravito-inertial waves also possess prograde and retrograde solution branches. In Figure 3, the prograde solutions are shaded blue and the retrograde waves pink. The solid purple curve is the bounding frequency between propagating and evanescent waves, and is obtained by setting $k_z = 0$ in the dispersion relation, Equation (20). The dashed black horizontal lines indicate the inertial frequency range, $\omega = \pm 2\Omega$, and the dotted black lines indicate the positive and negative values of the buoyancy frequency, $\omega = \pm N$. The two green dotted–dashed curves correspond to the prograde and retrograde f modes.

Separate dispersion relations can be developed for the acoustic waves and the gravito-inertial waves by considering high- and low-frequency limits of the full dispersion relation. In the high-frequency limit, we ignore those terms that have the frequency ω in the denominator, producing the following dispersion relation:

$$\omega^2 \approx (k_x^2 + k_z^2)c^2 + \omega_c^2 + 4\Omega^2. \tag{23}$$

The primary rotational modification to the p modes is a slight increase in the acoustic cutoff frequency that affects the prograde and retrograde solutions in the same manner. The low-frequency gravito-inertial waves are obtained by neglecting the terms $(\omega^2 - 4\Omega^2)/c^2$,

$$k_z^2(z) \approx -k_c^2 - k_x^2\left(1 - \frac{N^2}{\omega^2}\right) + \frac{2\Omega k_x}{\omega \mathcal{H}}, \tag{24}$$

where we have defined a cutoff wavenumber, k_c, that depends purely on the density stratification

$$k_c^2(z) \equiv \frac{\omega_c^2}{c^2} = \frac{1 - 2H'}{4H^2}. \tag{25}$$

3.1. Low-frequency Gravito-inertial Waves

The low-frequency version of the local dispersion relation (24) can be solved for the temporal frequency ω as long as we keep in mind that all of the atmospheric profiles and the radial wavenumber are functions of height but the frequency is a global, constant property. Equation (24) is quadratic in the frequency; hence, there are two solutions given by

$$\omega = \frac{k_x \Omega}{K^2 \mathcal{H}}\left[1 \pm \left(1 + K^2 \mathcal{H}^2 \frac{N^2}{\Omega^2}\right)^{1/2}\right], \tag{26}$$

where we have defined a wavenumber K,

$$K^2(z) \equiv k_x^2 + k_z^2(z) + k_c^2(z), \tag{27}$$

that is related to the total wavenumber of the wave, but includes a modification for stratification (through k_c^2). The nature of the two solutions depends explicitly on the relative importance of the restoring forces of buoyancy and the Coriolis force. We will examine the possible extremes in the next two subsections.

3.1.1. Limit of Slow Rotation

First, consider the situation where the magnitude of the buoyancy frequency is enormous compared to the rotation rate, $\Omega/|N| \ll 1$. In a low-mass star, such conditions occur both above and below the convection zone, within the outer atmosphere and within the radiative interior, as is illustrated in Figure 2(a). In these regions, the ratio of frequencies, $\Omega/|N|$, can be treated as a small parameter and we may expand the low-frequency dispersion relation (24) for slow rotation rates

(or strong buoyancy), finding

$$\omega = \pm\frac{k_x}{K}N + \frac{k_x\Omega}{K^2\mathcal{H}} + \cdots . \tag{28}$$

We have kept only the first two terms in the expansion and neglected all terms of order $(\Omega/N)^3$ or smaller. In a stably stratified atmosphere ($N^2 > 0$), the two solutions correspond to internal gravity waves that propagate in either the prograde or retrograde directions. In an unstable stratification, both solutions are unstable convective modes that propagate slowly prograde due to rotation. Of course, the effects of stratification arise from the buoyancy frequency N, but they also manifest through the wavenumber K that appears in the denominator of the first term in the expansion. Each wave has a small correction arising from the Coriolis force that has the familiar form $mC\Omega$, where $C = 1/(K^2R\mathcal{H})$ is a parameter depending on the stratification and wavenumbers. Since the sign of the correction is the same for both the prograde and retrograde solutions, the prograde mode propagates slightly faster than the retrograde gravity wave.

Figure 3(a) provides a propagation diagram for an isothermal atmosphere that is representative of the slow rotation limit (here with $\Omega/N = 0.2$). The prograde and retrograde branches are only weakly asymmetric, with the Coriolis force introducing the largest anisotropy at low zonal wavenumber, k_x. As the zonal wavenumber becomes large, the propagation band approaches that expected for internal gravity waves, $|\omega| < N$. We note that the expansion that appears in Equation (28) is valid not only in the limit of slow rotation, but also in the limit of short zonal wavelength, $\Omega/|N| \ll K\mathcal{H} \approx k_x\mathcal{H}$. Thus, for sufficiently large values of the zonal wavenumber, the buoyancy frequency term will dominate and the gravito-inertial waves behave like internal gravity waves.

3.1.2. Limit of Rapid Rotation

The converse limit, where the rotation rate is much larger in magnitude than the buoyancy frequency, may hold in a star's convection zone where efficient convection drives the unstable stratification toward neutral stability. Of course, the stratification remains slightly unstable, $N^2 < 0$, and the buoyancy frequency itself is purely imaginary. If we consider the limit of rapid rotation (or equivalently, weak buoyancy), $\Omega/|N| \gg K\mathcal{H}$, we find two gravito-inertial waves with very different natures. One is a prograde-propagating, almost pure, inertial oscillation, i.e., a thermal Rossby wave, with a frequency given by

$$\omega = \frac{2\Omega k_x}{K^2\mathcal{H}} + \frac{k_x\mathcal{H}}{2}\frac{N^2}{\Omega} + \cdots, \tag{29}$$

where we have neglected all terms of order $(N/\Omega)^4$ or smaller. The other solution is a slowly propagating gravito-inertial wave of mixed character,

$$\omega = -\frac{k_x\mathcal{H}}{2}\frac{N^2}{\Omega} + \cdots, \tag{30}$$

where we have kept only the first nonzero term in the expansion. For a stable stratification with $N^2 > 0$, like an isothermal atmosphere, the slow gravito-inertial wave is retrograde-propagating. For completeness, this situation is illustrated in Figure 3(b), but we recognize that this rapidly rotating limit never occurs in the stably stratified regions of a star. In an unstable stratification where $N^2 < 0$, the slow gravito-inertial wave is prograde. Hence, in a stellar convection zone, both the fast and slow gravito-inertial waves are prograde with positive frequencies.

The reader should note that the slow gravito-inertial wave approaches zero frequency in the limit of neutral stability ($N^2 \to 0$). Thus, in such an isentropic atmosphere, one of the solution branches corresponds to a prograde thermal Rossby wave and the other to a geostrophic mode that is stationary in the rotating frame of reference.

3.2. Wave Cavities and Turning Points

The gravito-inertial waves described by Equations (19) and (24) are radially propagating wherever the local wavenumber is purely real, $k_z^2 > 0$, and evanescent where it is imaginary, $k_z^2 < 0$. A wave cavity therefore exists wherever $k_z^2 > 0$, and the boundaries of that cavity correspond to the turning points of the equation where $k_z^2(z) = 0$. As we shall soon see, for low-mass stars this can result in two potential cavities: one in the convection zone and one in the radiative interior. These cavities are in fact waveguides, with waves trapped in radius and freely propagating in the zonal direction.

To see where a wave cavity exists, we need to consider the sign of each term in the local dispersion relation. Because $\mathcal{H} > 0$ and $-k_c^2 < 0$ (the density scale height H decreases with radius in a star, so $H' < 0$), only two of the terms in the local dispersion relation are potentially positive. We rewrite the low-frequency dispersion relation (24), moving these two terms to the front of the right-hand side, in order to emphasize which terms produce wave propagation:

$$k_z^2 = \left[\frac{2\Omega k_x}{\omega\mathcal{H}} + k_x^2\frac{N^2}{\omega^2}\right] - (k_x^2 + k_c^2). \tag{31}$$

For a wave cavity to exist, the term in the square brackets must exceed $k_x^2 + k_c^2$. Clearly, this can happen for low, real-valued frequencies. The first term, the Coriolis term, is large for frequencies less than the rotation rate, and it is responsible for inertial wave cavities. In order for this term to be positive, the waves must be prograde ($\omega/k_x > 0$). The second term, the buoyancy term, is large for frequencies less than the buoyancy frequency, and it results in a cavity for internal gravity waves. Both prograde and retrograde gravity waves are possible, but the term leading to radial propagation is positive only when the atmosphere is stably stratified $N^2 > 0$. If both terms are large, a cavity of mixed gravito-inertial waves results. Finally, we note that, even in an unstably stratified atmosphere, $N^2 < 0$, the Coriolis term can dominate the buoyancy term for sufficiently long wavelengths and for rapid enough rotation. These overstable convective modes have been stabilized by rotation and have been suggested as a possible mechanism for the excitation of the pulsation of β Cephei stars (Osaki 1974; Lee & Saio 1986, 1987) through coupling to gravity modes with similar frequency that reside in the overlying stably stratified outer envelope.

Since the buoyancy frequency dominates the rotation rate in a star's radiative interior, the resulting wave cavity is the well-known g-mode cavity with small corrections for the Coriolis force. In the deep interior, the cutoff wavenumber is much smaller than any reasonable zonal wavenumber, $k_c \ll k_x$. Hence, a bounding frequency for radial propagation can be

found by setting $k_z^2 = 0$ in the dispersion relation that is valid for slow rotation, Equation (28). Under these conditions, $K^2 = k_x^2 + k_z^2 + k_c^2 \approx k_x^2$, and propagation occurs for frequencies below the resulting bound:

$$|\omega| < N \pm \frac{\Omega}{k_x \mathcal{H}} + \cdots. \tag{32}$$

The positive sign refers to the prograde g mode and the negative sign to the retrograde mode.

In a star's convection zone, if we can ignore the buoyancy frequency ($N^2 = 0$), we expect a prograde thermal Rossby wave. We can easily demonstrate that a cavity exists for sufficiently rapid rotation. For an isentropic stratification, the scale height $\mathcal{H}$ reduces to the density scale height, $\mathcal{H} = H$. Further, the density scale height is an increasing function of depth within a star (because the temperature increases inward). Therefore, the positive Coriolis term in the dispersion relation, $2\Omega k_x/\omega H$, becomes small deep within the star, and at some depth below the photosphere, there exists a lower turning point where

$$\frac{2\Omega k_x}{\omega H} \approx k_x^2. \tag{33}$$

At this depth, downward-propagating thermal Rossby waves are refracted back upward toward the photosphere. Similarly, near the photosphere, where H becomes small and $k_c^2 = (1 - 2H')/4H^2$ becomes large, there is an upper turning point where

$$\frac{2\Omega k_x}{\omega H} \approx k_c^2. \tag{34}$$

At this height, an upward-traveling inertial wave is reflected downward. The inertial waves are therefore trapped between these two turning points, and the region in between coincides with the wave cavity. The general condition for radial propagation throughout a stellar convection zone can be expressed in terms of the temporal frequency through the following inequality:

$$\omega < \frac{2k_x\Omega}{(k_x^2 + k_c^2)H} + \cdots. \tag{35}$$

4. Inertial Waves in a Neutrally Stable Stratification

Stellar convection is exceedingly efficient in transporting heat, and the resulting outward heat flux drives the stratification of the convection zone toward neutral stability. Thus, a commonly adopted model for a stellar convection zone is an isentropic atmosphere for which $N^2 = 0$. The buoyancy force vanishes in such an atmosphere, and the waves become pure inertial oscillations, greatly simplifying the behavior of the wave field. Thus, we will examine inertial-wave propagation in an isentropic stratification in some detail.

A neutrally stable atmosphere is a special case of a polytropic atmosphere. For our purposes, it is sufficient to define a polytropic atmosphere as one that possesses a constant vertical temperature gradient, $T_0' = -Q$, and a corresponding temperature profile that is a linear function of height,

$$T_0 = -Qz. \tag{36}$$

In this expression, we have chosen to place the origin at the height where the linear temperature profile vanishes. The polytropic atmosphere only exists in the half-space below the origin, $z < 0$, where the temperature is positive. For an ideal gas in a plane-parallel atmosphere with constant gravity, such a temperature gradient results in power-law relations for the thermodynamic variables:

$$\rho_0(z) = A\,(-z)^\alpha, \tag{37}$$

$$P_0(z) = \frac{gA}{\alpha + 1}(-z)^{\alpha+1}, \tag{38}$$

$$c^2(z) = \frac{\gamma g(-z)}{\alpha + 1}. \tag{39}$$

Here, A is an arbitrary constant and α is a dimensionless parameter called the polytropic index, which is related to the temperature gradient, Q:

$$\alpha = \frac{g}{R_{\rm gas} Q} - 1. \tag{40}$$

The density scale height H, the buoyancy frequency N, and cutoff wavenumber k_c similarly are power laws:

$$H = \frac{(-z)}{\alpha}, \tag{41}$$

$$N^2 = \frac{\alpha - \hat{\alpha}}{\gamma\hat{\alpha}}\frac{g}{(-z)}, \tag{42}$$

$$k_c^2 = \frac{\alpha(\alpha + 2)}{4z^2}. \tag{43}$$

The quantity $\hat{\alpha}$ that appears in the expression for the buoyancy frequency is the value of the polytropic index that corresponds to neutral stability, $\hat{\alpha} \equiv (\gamma - 1)^{-1}$. For a fully ionized, monatomic gas with $\gamma = 5/3$, this corresponds to a polytropic index of $\hat{\alpha} = 3/2$.

4.1. Wave Cavity for a Neutrally Stable Polytrope

In the limit of neutral stability, the local dispersion relationship that describes low-frequency inertial waves, Equation (24), simplifies significantly:

$$k_z^2(z) = \frac{2\Omega k_x}{\omega H} - k_x^2 - k_c^2 = -\frac{2\kappa k_x}{z} - k_x^2 - \frac{\alpha(\alpha + 2)}{4z^2}. \tag{44}$$

In the final expression, κ is a constant defined by

$$\kappa \equiv \frac{\alpha\Omega}{\omega}. \tag{45}$$

The turning points that demark the boundaries of the inertial wave cavity can be found by setting $k_z^2 = 0$ in the local dispersion relation and solving the resulting quadratic equation for the two roots in z,

$$z_{\rm turn} = -k_x^{-1}\left[\kappa \pm \sqrt{\kappa^2 - \frac{\alpha(\alpha + 2)}{4}}\right]. \tag{46}$$

The negative sign generates the upper turning point and the plus sign the lower turning point. From this expression for the turning points, we can derive a necessary condition for the existence of a wave cavity. Two real roots must exist, and this

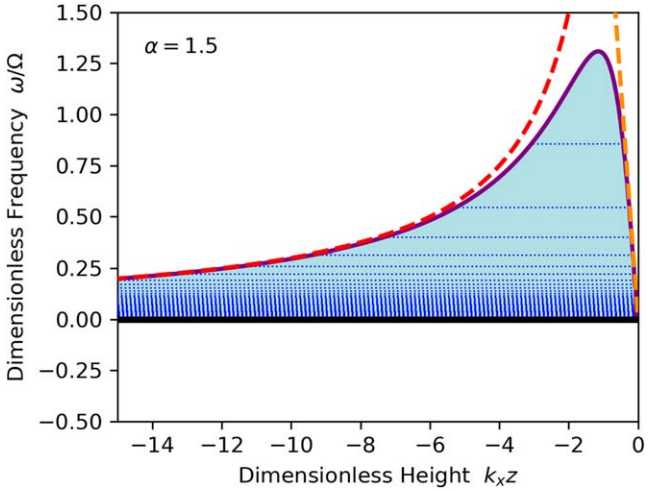

Figure 4. Propagation diagram for thermal Rossby waves in an atmosphere that is neutrally stable to convective overturning. At each height in the atmosphere, the frequencies of waves that are vertically propagating are shaded pale blue. All such waves have positive frequencies and propagate longitudinally in a prograde direction (in the rotating reference frame). The solid purple curve indicates the upper frequency bound for radial propagation. If one draws a horizontal line at a specific frequency, the two points where this line crosses the upper bound denote the turning points and the blue shaded region in between corresponds to the inertial-wave cavity. The red and orange dashed lines are approximations to the upper frequency bound that are valid deep in the atmosphere (red) and near the upper surface (orange)—see the text, Equation (49). The thin, horizontal, blue, dotted lines mark the eigenfrequencies of the thermal Rossby modes.

requires that the argument of the square root is positive:

$$\omega < \sqrt{\frac{\alpha}{\alpha + 2}}\, 2\Omega. \tag{47}$$

Therefore, for an inertial wave cavity to exist, the frequency must lie below a cutoff that depends on both the rotation rate Ω and on the stratification (through the polytropic index α). For a neutrally stable polytrope with $\alpha = 1.5$, the frequency must satisfy $\omega \lesssim 1.3\ \Omega$.

A convenient form of the local dispersion relation can be obtained by defining a dimensionless depth, $\zeta = -2\, k_x z$, that scales the vertical coordinate with the zonal wavenumber. The factor of two is included purely for convenience in subsequent equations. Using this spatial variable, the local dispersion relation can be written in the following form:

$$\frac{k_z^2(z)}{k_x^2} = \frac{4\alpha}{\zeta}\frac{\Omega}{\omega} - 1 - \frac{\alpha(\alpha + 2)}{\zeta^2}. \tag{48}$$

As one can see, the zonal wavenumber drops out of the right-hand side. This allows us to plot the propagation band as a function of a dimensionless frequency, ω/Ω, and dimensionless depth, ζ, for any zonal wavenumber, capturing all of the behavior in a single diagram. As the zonal wavenumber changes, the shape of the cavity does not change, but its vertical extent scales with the wavelength. Figure 4 shows such a propagation diagram for an $\alpha = 1.5$ neutrally stable polytrope. All of the vertically propagating waves are prograde thermal Rossby waves (blue shaded region in Figure 4) because the retrograde branch is degenerate at zero frequency for a neutrally stable atmosphere.

In Figure 4, the dashed red and orange curves illustrate the effects of refraction and reflection in determining the turning points. Deep in the atmosphere, the balance is that of Equation (33), where the Coriolis term balances k_x^2 in the local dispersion relation. The red curve is given by solving this balance for the frequency,

$$\omega \approx \frac{2\Omega}{k_x H} = -\frac{2\alpha\Omega}{k_x z}. \tag{49}$$

From this expression, it is obvious that waves of different frequency have different turning points. Solving for the lower turning point, $z_{\rm lower}$, we obtain

$$z_{\rm lower} \approx -k_x^{-1}\frac{2\alpha\Omega}{\omega}. \tag{50}$$

In particular, low-frequency waves have a much deeper lower turning point, and in the limit $\omega \to 0$, the lower turning point becomes infinitely deep.

Similarly, the orange curve in Figure 4 corresponds to the frequencies obtained by balancing the Coriolis term with k_c^2—as in Equation (34)—which is the balance that holds very close to the outer surface. The resulting frequency and the concomitant upper turning point, $z_{\rm upper}$ are given by

$$\omega \approx \frac{2\Omega k_x}{k_c^2 H} = -\frac{8\Omega k_x z}{\alpha + 1}, \tag{51}$$

$$z_{\rm upper} \approx -k_x^{-1}\frac{(\alpha + 1)\omega}{8\Omega}. \tag{52}$$

Lower frequencies have cavities that reach closer to the surface. However, since inertial waves are restricted to frequencies less than 2Ω, the upper turning point can never extend very deeply: $z_{\rm upper} > -(\alpha + 1)/4k_x$.

Since the depth of the lower turning point scales inversely with the zonal wavenumber (see Equation (50)), waves with a short zonal wavelength are trapped just below the surface. Hence, these waves do not sense the spherical geometry of the star, nor the radial variation of its gravitational acceleration. We can see that our a priori neglect of these two effects are justified a posteriori in the limit of short zonal wavelengths.

4.2. Analytic Solution for a Neutrally Stable Polytrope

When the atmosphere is polytropic, the standard form of the wave equation reduces to a well-studied ODE, namely Whittaker's Equation. To illustrate this, in Equations (19) and (44), we make a change of variable to the nondimensional depth that we introduced earlier, $\zeta \equiv -2k_x z$:

$$\frac{d^2\Psi}{d\zeta^2} + \left[\frac{\kappa}{\zeta} - \frac{1}{4} + \frac{1/4 - \mu^2}{\zeta^2}\right]\Psi(z) = 0, \tag{53}$$

with the definition

$$\mu \equiv \frac{\alpha + 1}{2}. \tag{54}$$

Note that both κ and μ are constants. The constant κ will serve as the eigenvalue of the ODE and it depends on the wave frequency—see Equation (45). We note that the definition of κ that appears in Equation (45) is only valid is the low-frequency regime of the local dispersion relation (44). The constant μ is a parameter that depends purely on the stratification. Equation (19) is Whittaker's

Equation (Abramowitz & Stegun 1964), which has two solutions, called Whittaker functions: $\mathcal{M}_{\kappa\mu}(\zeta)$ and $\mathcal{W}_{\kappa\mu}(\zeta)$. These Whittaker functions can be expressed in terms of Kummer's confluent hypergeometric functions of the first and second kind, M and U (confusingly, these are sometimes referred to as Kummer's function and Tricomi's function, respectively),

$$\mathcal{M}_{\kappa\mu}(\zeta) = e^{-\zeta/2}\,\zeta^{\mu+1/2}\,M(-\eta,\,1+2\mu,\,\zeta), \tag{55}$$

$$\mathcal{W}_{\kappa\mu}(\zeta) = e^{-\zeta/2}\,\zeta^{\mu+1/2}\,U(-\eta,\,1+2\mu,\,\zeta), \tag{56}$$

where $\eta \equiv \kappa - (\mu + 1/2)$. The general solution for the Lagrangian pressure fluctuation is therefore a linear combination of these two solutions,

$$\delta\varpi(z) = \rho_0^{-1/2}\,\Psi(z) = z\,e^{k_x z}[C_a M(-\eta,\,\alpha+2,\,-2k_x z) + C_b U(-\eta,\,\alpha+2,\,-2k_x z)], \tag{57}$$

with arbitrary constants C_a and C_b whose ratio is determined by the boundary conditions.

4.3. Boundary Conditions and Eigenmodes

When physically appropriate boundary conditions are applied in height, Whittaker's Equation generates a discrete spectrum of eigenmodes, with κ serving as the eigenvalue. Since κ is a function of the frequency, each eigenmode will possess a specific eigenfrequency,

$$\omega_n = \frac{\alpha\Omega}{\kappa_n}, \tag{58}$$

where n is the radial order of the mode and $\kappa_n = \kappa_n(k_x)$ is the nth eigenvalue, which is potentially a function of the zonal wavenumber.

4.3.1. Eigenmodes for a Semi-infinite Polytrope

Whittaker's equation has two singular points, one at the origin $\zeta = 0$ (i.e., at the upper surface of the polytrope, $z = 0$) and the other at infinity $\zeta \to \infty$ (or $z \to -\infty$). In this subsection, we will model the convection zone of a star as a semi-infinite polytropic layer that extends between these two singular points. Obviously, a star's convection zone has a finite depth. But, as we have already discussed, the wave cavity is confined to a region near the upper surface and the depth to which this cavity extends is proportional to the zonal wavelength of the wave. Thus, if the zonal wavelength is sufficiently short, the lower turning point of the wave may be many e-folding lengths from the physical boundary at the bottom of the convection zone. Hence, such waves do not sense the bottom and we can treat the domain as semi-infinite. In the subsequent subsection, Section 4.3.2, we will consider what happens when the eigenfunctions begin to reach deeply enough to be influenced by the lower boundary.

If we apply boundary conditions of regularity at the origin and at infinity (at the two singular points), the solution simplifies dramatically. The U confluent hypergeometric function is badly divergent at the origin, so we reject it. The M confluent hypergeometric function is divergent at infinity unless the eigenvalue κ takes on specific discrete values. Explicitly, the parameter η must be a nonnegative integer,

$$\eta_n = \kappa_n - (\mu + 1/2) = n, \qquad n \in 0,\,1,\,2,\,3,\ldots. \tag{59}$$

For these integer values of η, the Kummer functions reduce to associated Laguerre polynomials, and to within an arbitrary constant amplitude, C_n, the eigenfunctions become

$$\delta\varpi_n(z) = C_n\,z\,e^{k_x z}\,L_n^{(\alpha+1)}(-2k_x z), \tag{60}$$

where $L_n^{(\alpha+1)}$ is the nth-order associated Laguerre polynomial.

For these boundary conditions, the eigenfrequencies have the unexpected property that they are insensitive to the zonal wavenumber. Inserting Equation (59) into Equation (58), we obtain a global dispersion relation that expresses the mode frequency as a function of only the radial order n, the rotation rate Ω, and the polytropic index α:

$$\omega_n = \frac{2\Omega}{1 + 2(n+1)/\alpha}. \tag{61}$$

In Section 5.4, we discuss in more detail why the eigenfrequencies for this set of boundary conditions are independent of the zonal wavenumber. But, in short, this property is the result of the self-similarity of a polytropic atmosphere and the boundary conditions; neither possesses an imposed spatial scale. In the next subsection, we will consider a finite spatial domain and discover that the self-similarity of the boundary conditions is broken and the eigenfrequencies will subsequently depend on the zonal wavenumber.

The eigenfrequencies are indicated in Figure 4 by plotting a horizontal dotted blue line at the frequency corresponding to each eigenmode. Each line extends between the two turning points, thus illustrating the spatial extent of the wave cavity for each eigenmode. As is typical for inertial oscillations, the lowest radial orders n possess the highest frequencies, and there is an accumulation point at zero frequency as the mode order becomes large ($n \to \infty$).

Figure 5 shows radial eigenfunctions for modes corresponding to the lowest four radial orders. The left panel shows the eigenfunction for the Lagrangian pressure fluctuation, scaled by ω/g such that the eigenfunctions have physical units of velocity. The right-hand panel of Figure 5 presents the corresponding eigenfunctions for the zonal velocity, Equation (15). We do not illustrate the vertical velocity separately, because the vertical velocity is nearly proportional to the reduced Lagrangian pressure fluctuation when in the low-frequency limit (see Section 5.2). In fact, in this low-frequency limit, the left-hand panel plots the imaginary component of the vertical velocity as well as the Lagrangian pressure fluctuation, as can be verified by taking the low-frequency limit of Equation (16). Each of the eigenfunctions has been normalized such that the zonal velocity has a maximum amplitude of unity that is achieved at the upper surface. In general, the zonal velocity is the larger of the two velocity components, but this is especially true near the upper surface. The vertical velocity vanishes at the upper boundary for all modes, while the zonal velocity reaches maximum amplitude at the surface. This is a result of the upper surface being a regular singular point of Whittaker's equation.

The wave cavity is different for each mode, and extends from the lower turning point, which is indicated in Figure 5 by the solid circular dot, to the upper turning point, which lies just below the upper boundary (not illustrated, for clarity). For the four radial modes that are shown, the upper turning points all

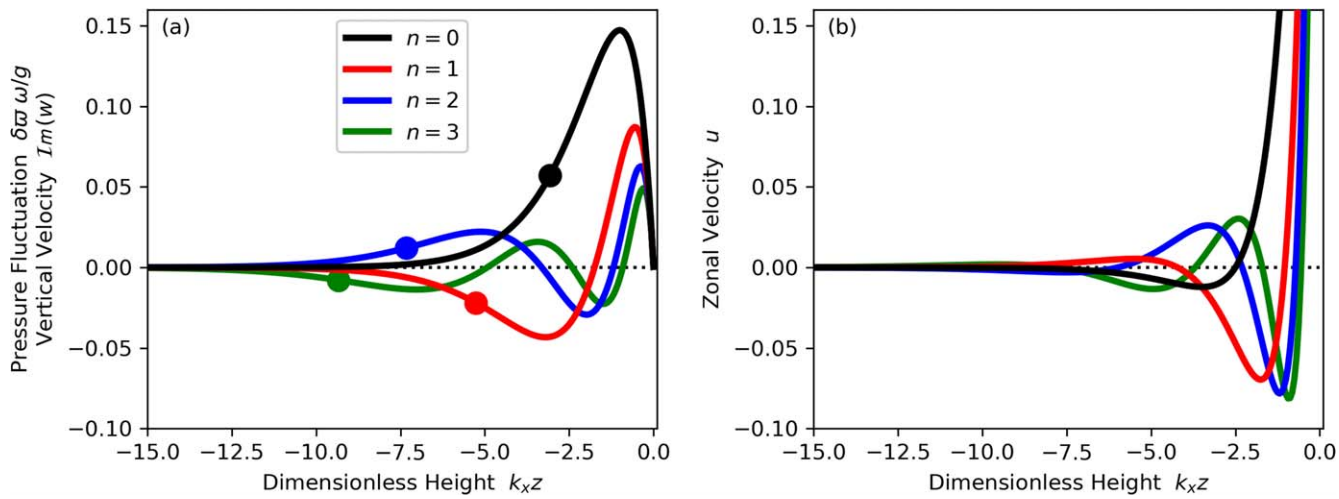

Figure 5. Radial eigenfunctions for a semi-infinite neutrally stable polytropic atmosphere. The two panels correspond to (a) the reduced Lagrangian pressure fluctuation $\delta\varpi$ and (b) the zonal velocity u. For modes like these with low frequency, the left-hand panel also indicates the imaginary part of the vertical velocity w. The first four radial modes with radial orders $n = 0$, 1, 2, and 3 are indicated by the color of the curve (black, red, blue, and green, respectively). The colored dots that appear on the eigenfunction curves indicate the location of the lower turning point of the wave cavity. The upper turning points are all very close to the upper boundary, $z = 0$, and are omitted for clarity. Note, the eigenfunctions only depend on the zonal wavenumber through a self-similar scaling of the vertical coordinate. Thus, these eigenfunctions are universal and apply to all modes of the relevant radial order, independent of the zonal wavelength.

lie very close to the upper surface and very near each other, with $k_x z_{\rm upper}$ ranging between -0.43 and -0.14.

4.3.2. Eigenmodes for a Polytropic Layer of Finite Depth

As can be seen in Figure 5, as the zonal wavelength increases or the frequency decreases, the eigenfunctions reach deeper and deeper into the star. Eventually, the eigenfunction becomes sensitive to the bottom of the convection zone. To test such effects, we consider a finite layer that spans the range of heights $z \in [-D, 0]$, where $D = 200$ Mm is approximately the depth of the Sun's convection zone. Hence, boundary conditions are applied at the singular point corresponding to the origin and at the regular point $z = -D$. As before, we require regularity at the upper surface. For simplicity, we require that the Lagrangian pressure fluctuation vanishes at the bottom of the convection zone, $\delta\varpi(-D) = 0$. This boundary condition is consistent with one of impenetrability $w = 0$ at low frequencies. As before, the boundary condition of regularity at $z = 0$, forces us to reject the U confluent hypergeometric function. The boundary condition at the bottom of the convection zone then generates a transcendental global dispersion relation involving the M Kummer function,

$$M(-\eta, \alpha + 2, 2k_x D) = 0. \tag{62}$$

We have solved this equation numerically for the discrete set of eigenvalues ($\eta = \eta_n$), and the results are shown in Figure 6. The solid black, red, blue, and green curves illustrate the mode frequencies for the radial fundamental $n = 0$ (black) and the first three overtones $n = 1$, 2, and 3 (red, blue, and green, respectively). The light blue curves represent all of the higher-order overtones, which have been left unlabeled for the sake of clarity. As expected, there is an accumulation point at zero frequency as $n \to \infty$, and this causes all of the pale blue curves to appear to merge into a solid band of color.

Two specific eigenmodes are marked along each of the first four dispersion curves. The diamond symbol corresponds to a mode with low wavenumber $m = k_x R_\odot = 10$, and the circular symbol to a higher wavenumber $m = 40$. The eigenfunctions for these modes are shown in Figure 7. The upper panels show the Lagrangian pressure fluctuation and the zonal velocity for the smaller wavenumber ($m = 10$), while the lower panels illustrate the same quantities for the larger wavenumber ($m = 40$).

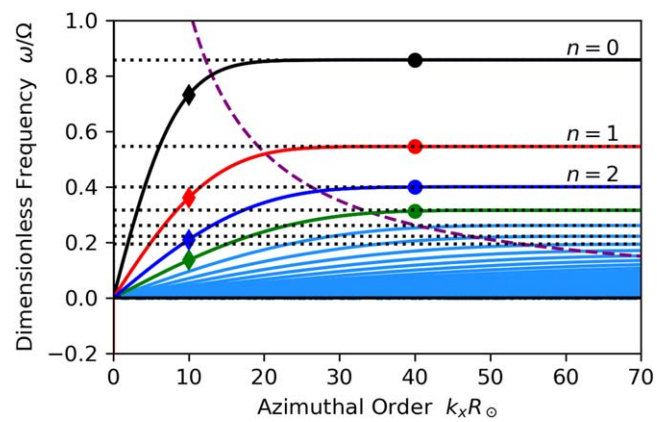

Figure 6. Eigenfrequencies for a neutrally stable layer of finite depth shown as a function of the zonal wavenumber k_x. The upper boundary of the layer is located at the origin, and the bottom of the layer is 200 Mm deep, mimicking the Sun's convection zone. At the upper boundary, we require that the solutions remain finite, and on the lower boundary, we impose a condition of impenetrability. The eigenfrequencies of the first four radial modes are shown with the black ($n = 0$), red ($n = 1$), blue ($n = 2$), and green ($n = 3$) curves. Higher-order overtones ($n > 3$) are drawn in pale blue. At very short zonal wavelengths (high k_x), the eigenfunctions do not sense the presence of the lower boundary. Hence, they have the same frequencies as the semi-infinite layer. These asymptotic frequencies are indicated with the dotted horizontal lines. As the wavenumber decreases (and the zonal wavelength grows), the lower edge of the wave cavity approaches the bottom of the domain and eventually crosses it. The frequency for which this crossing occurs is indicated by the dashed purple curve. For wavenumbers less than this threshold, the eigenfunctions (and eigenfrequencies) are strongly influenced by the lower boundary condition, and the frequency decreases linearly toward zero frequency at zero wavenumber. Along the first four dispersion curves are marked two modes. The diamonds indicate modes with wavenumber $k_x R_\odot = 10$, and the circles correspond to modes with $k_x R_\odot = 40$. The eigenfunctions for these modes are illustrated in Figure 7.

At low values of the zonal wavenumber, the frequency along a single dispersion curve increases linearly with wavenumber.

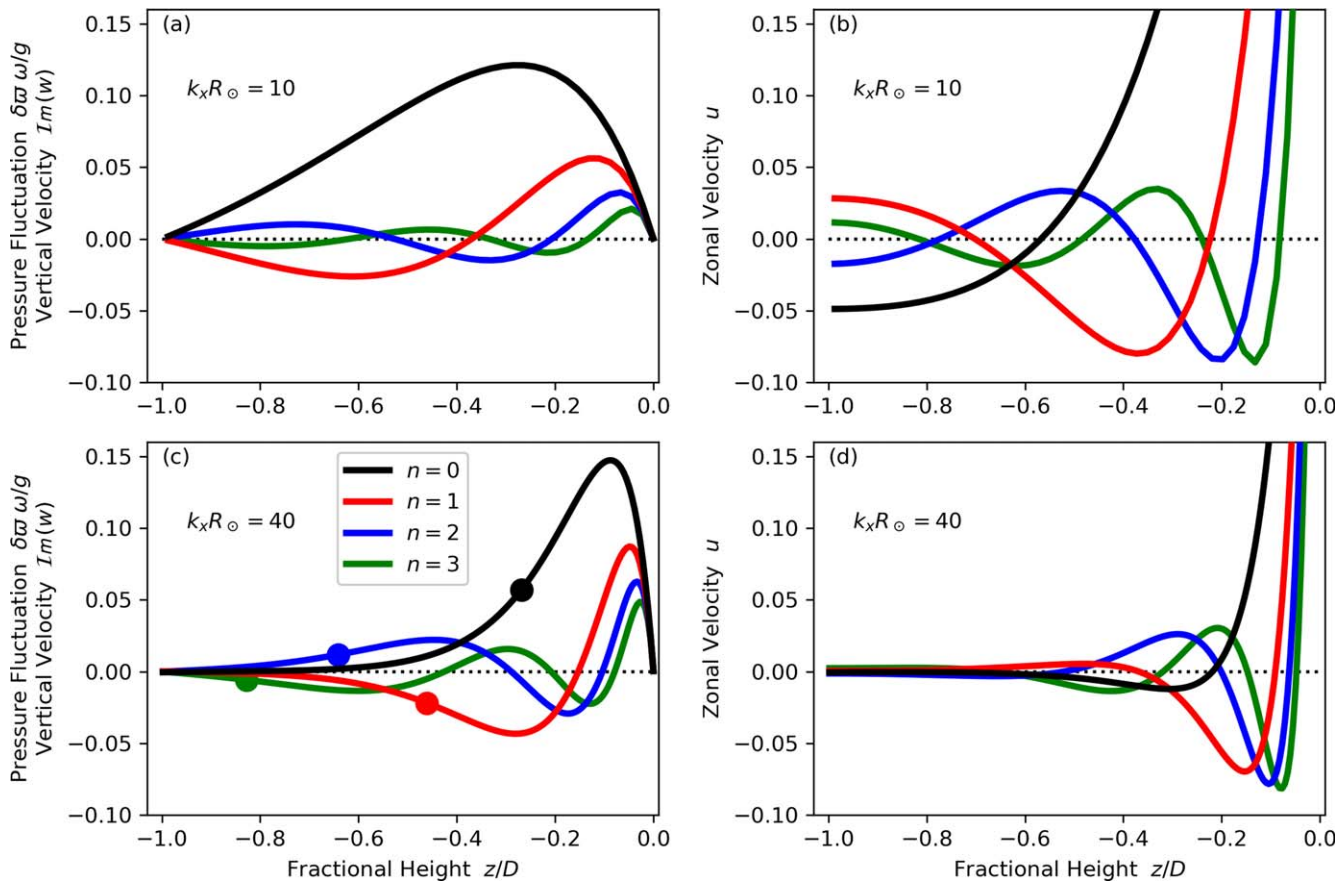

Figure 7. Eigenfunctions for the modes indicated by the diamonds (top panels) and circles (bottom panels) that appear in Figure 6. The upper panels correspond to modes with a low zonal wavenumber given by $k_xR_\odot = 10$, and the lower panels to a larger wavenumber $k_xR_\odot = 40$. The left-hand panels, (a) and (c), show the vertical variation of the reduced Lagrangian pressure fluctuation, $\delta\varpi(z)$, and simultaneously the imaginary part of the vertical velocity $w(z)$. The right-hand panels, (b) and (d), present the zonal velocity $u(z)$. The eigenfunctions for first four radial orders, $n = 0$, 1, 2, and 3, appear as the black, red, blue, and green curves, respectively. Using the same color scheme, the lower turning point for each mode is indicated by a large circular dot. For the modes that appear in the upper panels, the lower turning point is below the lower boundary—and thus unillustrated outside the solution domain.

This is the wavenumber regime in which the lower turning point of the wave equation lies below the lower boundary, $z_{\rm lower} < -D$. Thus, the eigenfunctions extend throughout the entirety of the finite domain, and the lower boundary condition has significant influence on the eigenmodes. The modes marked with the diamond symbols in Figure 6 are all within this regime, and one can see that their eigenfunctions remain propagating all the way to the bottom of the spatial domain.

As the wavenumber becomes larger, the lower turning point eventually crosses the lower boundary and passes into the solution domain. We can approximate the frequency for which the lower turning point and the lower boundary are coincident ($z_{\rm lower} = -D$) by using Equation (50),

$$\frac{\omega}{\Omega} \approx \frac{2\alpha}{k_x D}. \tag{63}$$

This transition frequency is shown in Figure 6 using the dashed purple curve. Further increase to the wavenumber results in the withdrawal of the wave cavity from the lower boundary, and the presence of that lower boundary becomes less and less important to the eigenmode. Hence, for sufficiently large wavenumbers (those that lie to the right of the dashed purple curve), the dispersion curves in Figure 6 asymptote to the constant frequencies associated with eigenmodes of the semi-infinite domain. These asymptotic values, Equation (61), are shown with the dotted lines. For the sake of clarity, dotted lines are shown only for the first seven modes. The eigenmodes that are indicated by the circular symbols all lie within this high-wavenumber regime and possess lower turning points that lie between the two boundaries. As such, their wave cavities do not extend all the way to the bottom of the convection zone. To illustrate this, Figure 7(d) indicates the lower turning point for each mode with an appropriately colored circular dot.

4.3.3. Eigenmodes for a Submerged Polytropic Layer

In this subsection, we consider a buried layer of finite radial extent that is fully submerged beneath the polytrope's singular upper surface. We place impenetrable boundaries at two depths, $z = -D$ and $z = -d$, with $D > d$. Thus, as in the previous subsection, the lower boundary is at $-D$, but now instead of being located at the origin, the upper boundary is at $-d$. Because neither of the ODEs' singular points lie within the spatial domain, $z \in [-D, -d]$, we must retain both of the confluent hypergeometric functions, and we must find the linear combination of M and U that causes the Lagrangian pressure fluctuation (or equivalently, at low frequencies, the vertical velocity) to vanish at both boundaries. This is readily accomplished by using a numerical root finder to obtain the

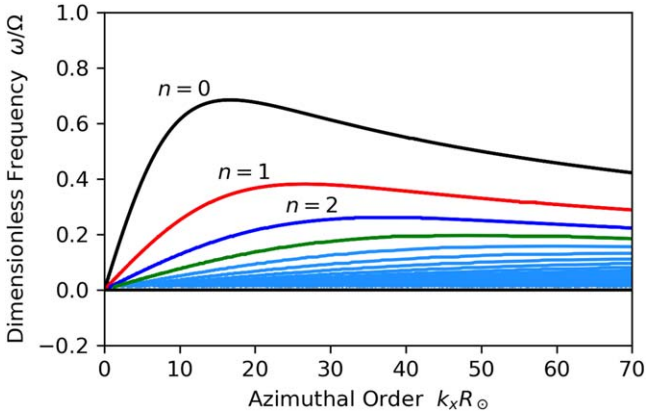

Figure 8. Eigenfrequencies as a function of zonal wavenumber k_x for a fully submerged polytropic layer with lower and upper boundaries at $z = -200$ Mm and $z = -30$ Mm, respectively. A condition of impenetrability is applied at both boundaries. The colors have the same meaning as in Figure 6. For low wavenumbers, the eigenfrequencies increase linearly, and this behavior is caused by the lower turning point being below the lower boundary of the convection zone. The upper boundary condition exerts its influence most strongly at large wavenumbers. For these modes, the upper turning point lies above the upper boundary of the domain, and the wave cavity is effectively truncated by the upper boundary condition. A smaller wave cavity requires smaller frequencies in order to squeeze the same number of vertical wavelengths within the cavity. Hence, at sufficiently large wavenumber, the eigenfrequencies decrease monotonically with increasing wavenumber as the wave cavity becomes increasingly truncated.

roots of the following matrix determinant:

$$\begin{vmatrix} M(-\eta,\, \alpha+2,\, 2k_x D) & U(-\eta,\, \alpha+2,\, 2k_x D) \\ M(-\eta,\, \alpha+2,\, 2k_x d) & U(-\eta,\, \alpha+2,\, 2k_x d) \end{vmatrix} = 0. \quad (64)$$

Figure 8 provides the resulting dispersion diagram for a model with $d = 30$ Mm and $D = 200$ Mm. The depression of the upper boundary condition below the singularity of the polytrope modifies the asymptotic behavior for large wavenumbers. Instead of approaching a constant value, the frequencies monotonically decrease after achieving a local maximum, which lies near the wavenumber marking the transition from low- to high-wavenumber regimes in Figure 6. This behavior arises because the size of the wave cavity is reduced for those waves that have an upper turning point that lies above the upper boundary $z_{\rm upper} > -d$. In order to fit the same number of vertical wavelengths within the reduced domain, the frequency must be decreased. Further, the truncation of the wave cavity is more severe for waves with a large zonal wavenumber, because the cavity is fundamentally thinner. This same frequency behavior was found previously by Glatzmaier & Gilman (1981), but they solved the ODE by using Frobenius expansions and presented solutions only for the radial fundamental $n = 0$.

5. Discussion

Under the assumptions of short longitudinal wavelengths and 2D motions perpendicular to the rotation axis, we have derived an ODE, Equation (18), that describes the propagation of atmospheric waves through an atmosphere with general stratification. There are two families of solutions: a high-frequency branch of acoustic waves and a low-frequency branch of gravito-inertial waves. From this governing ODE, we have derived a local dispersion relation and have demonstrated that in the absence of buoyancy the thermal Rossby waves are trapped radially in a waveguide that is confined to the upper reaches of the convection zone. The upper boundary of this waveguide is caused by reflection of an upward-propagating wave by the density stratification—specifically, when the vertical wavelength becomes comparable to the density scale height. This reflection is substantiated in the dispersion relation by a cutoff wavenumber that is related to the acoustic cutoff frequency. The lower boundary of the waveguide is caused by the upward refraction of obliquely propagating wave fronts as the wave propagates downward into a region with increasing density scale height. Due to the refractive nature of this turning point, waves with shorter longitudinal wavelengths (large k_x) have a shallower wave cavity and are trapped closer to the upper boundary.

5.1. Location of the Waveguide

The exact location of the cavity for thermal Rossby waves is rather sensitive to the superadiabatic gradient. We have shown that, for a neutral stratification, $N^2 = 0$, the cavity is in the upper portion of the convection zone. This result is robust as long as the magnitude of the buoyancy frequency is small compared to the rotation rate. Unfortunately, this condition is unlikely to hold true for the solar-like stars. Figure 2 presents the buoyancy frequency in a standard model of the Sun's internal structure, i.e., Model S of Christensen-Dalsgaard et al. (1996). The left-hand panel shows the square of the buoyancy frequency throughout the Sun's interior (blue curve). The convection zone corresponds to the region where the square of the buoyancy frequency is negative. For reference, the Sun's Carrington rotation rate, $\Omega_\odot = 2.87 \times 10^{-6}\ {\rm s}^{-1}$, is indicated by the two red horizontal lines (located at $\omega^2 = \pm\Omega_\odot^2$). The figure suggests that the upper and lower halves of the convection zone are in converse regimes. The upper convection zone is in the slow rotation limit where $|N| \gg \Omega$ and the deeper portion of the convection zone is in the limit of rapid rotation, $|N| \ll \Omega$. If this suggestion is true, the upper portion of the convection zone is inherently unstable for waves of all wavelengths, but the lower portion of the convection zone might support stable thermal Rossby waves—or equivalently, overstable convective modes—if their wavelengths are sufficiently long. How long? An estimate can be derived from the local dispersion relation, Equation (26), by requiring that the temporal frequency is purely real. When the square of the buoyancy frequency is negative, this provides a restriction on the wavenumber:

$$k_x^2 + k_z^2 < \frac{\Omega^2}{\mathcal{H}^2 |N^2|} - k_c^2. \quad (65)$$

Deep in the convection zone, we can ignore k_c^2 and $\mathcal{H} \approx H$, resulting in the following expression for the wavelength, λ:

$$\frac{\lambda}{2\pi} = (k_x^2 + k_z^2)^{-1/2} = H\frac{|N|}{\Omega}. \quad (66)$$

From Figure 2, we estimate that, at the base of the convection zone, the ratio of the buoyancy frequency to the rotation rate has a typical value of $|N|/\Omega \sim 0.1$. Further, at the base of the convection zone, the density scale height is roughly 100 Mm. Therefore, for local stability, the gravito-inertial waves must have wavelengths longer than 60 Mm ($\sim 2\pi \times 0.1 \times 100$ Mm). For waves with similar longitudinal and vertical wavelengths, such waves would have azimuthal orders $m \lesssim 30$.

The existence of a deep cavity for overstable convective modes in the Sun remains rather speculative for a variety of reasons. First, the wavelength bound that we just estimated is sufficiently large that our short-wavelength approximation is beginning to fray. Second, the stability condition is purely a local one. Calculating global stability would require solving the eigenvalue problem for a solar-like stratification. Third, while the sound speed and density profile of Model S (and other solar models) have been tested very well by helioseismology, the superadiabaticity in the convection zone remains poorly constrained. Helioseismology can only place a rather large upper limit, and the buoyancy frequency could be much smaller in magnitude and remain consistent with observations. In most solar models, the superadiabaticity is completely determined by mixing-length theory. The entropy gradient is fixed by the requirement that the convective heat flux carries a solar luminosity through the convection zone. Thus, the modeled buoyancy frequency in the convection zone is only as reliable as mixing-length theory is in detailed modeling of the convective heat transport.

5.2. The Anelastic Limit

Even though internal gravity waves are usually much lower in frequency than acoustic waves, compressibility is still important for their propagation. Hence, anelastic treatments of the continuity equation, where the mass flux is assumed to be divergenceless, $\boldsymbol{\nabla}\cdot(\rho_0\boldsymbol{u})\approx 0$, often cause internal gravity waves to fail to conserve energy (Brown et al. 2012). This is the primary reason that here we have adopted a continuity equation appropriate for a completely compressible fluid. Despite these well-known issues for internal gravity waves, one still hopes that anelasticity should hold in the limit of slowly evolving motions, i.e., for low frequencies. Satisfyingly, this proves to be true. If we assume that the waves of interest have very low frequency, $\omega^2 \ll gk_x$, we may consider limits of Equations (15) and (16) under the condition that $\omega^2 \ll \sigma^2$. To leading order, we obtain:

$$u \approx -\frac{\omega}{gk_x - 2\Omega\omega}\left(\frac{d}{dz} - \frac{1}{H}\right)\delta\varpi, \tag{67}$$

$$w \approx \frac{i\omega k_x}{gk_x - 2\Omega\omega}\,\delta\varpi. \tag{68}$$

If one works their way back through the derivation of Equations (15) and (16), one can determine that this low-frequency approximation is equivalent to neglecting the inertial term that appears on the left-hand side of the momentum Equation (9). These equations demonstrate that very low-frequency waves can be expressed using a stream function for the mass flux:

$$\rho_0 u \approx -\frac{d\psi}{dz}, \tag{69}$$

$$\rho_0 w \approx \frac{d\psi}{dx}, \tag{70}$$

$$\psi \equiv \frac{\omega}{gk_x - 2\Omega\omega}\,\rho_0\delta\varpi, \tag{71}$$

where the stream function is proportional to the reduced Lagrangian pressure fluctuation. Therefore, the mass flux must be divergenceless $\boldsymbol{\nabla}\cdot(\rho_0\boldsymbol{u})\approx 0$, and the anelastic approximation is satisfied. Further, by using Equation (13) to express the Lagrangian pressure fluctuation in terms of the Eulerian fluctuation, one can demonstrate that these very low-frequency anelastic flows are geostrophic to leading order:

$$\rho_0 u \approx \frac{1}{2\Omega}\frac{dP_1}{dz}, \tag{72}$$

$$\rho_0 w \approx -\frac{1}{2\Omega}\frac{dP_1}{dx}. \tag{73}$$

For very low—but nonzero—frequencies, inertia and buoyancy appear as higher-order perturbations to geostrophic balance, and it is the dynamics of these perturbations that lead to prograde propagation of the flow pattern.

5.3. Geometry of the Eigenfunctions

The eigenfunctions that we illustrate in Figures 5 and 7 correspond to a longitudinal sequence of rolls aligned with the rotation axis. In order to illustrate this geometry, we provide Figure 9, which shows the 2D motion for four distinct eigenfunctions. The upper panels correspond to the fundamental radial eigenmode, $n = 0$, and the bottom panels to the first radial overtone, $n = 1$. The right and left panels provide eigenfunctions for two different zonal wavenumbers: a small wavenumber $m = k_x R_\odot = 40$ on the left, and a larger wavenumber $m = 80$ on the right. In each panel, longitude runs from right to left, and the outer surface of the star's convection zone lies at the top, with the center of the star located downward beyond the bottom of each panel. The reader's viewpoint is consistent with looking down upon a piece of the star's equatorial plane from above the north pole.

The colored images in Figure 9 illustrate the stream function, ψ, for the eigenfunction's mass flux. The black curves mark the isocontours of the stream function, and hence, indicate the flowlines. Red tones and dashed isocontours correspond to negative values of the stream function resulting in clockwise flow along the isocontours (anticyclonic motion). Conversely, the blue tones and solid curves indicate positive values of the stream function and counterclockwise, cyclonic flow. The thick black lines indicate the zero contours, or the boundaries between cells. The flow field is composed of parallel rolls whose axes are all aligned with the star's rotation vector. A single zonal wavelength consists of two counterrotating rolls, one clockwise and the other counterclockwise.

As expected, the fundamental mode consists of a single roll in depth while the first radial overtone possesses two counterrotating rolls stacked in depth. The upper roll looks weak in these renditions. This is an artifact of the stream function generating the mass flux instead of the velocity field itself. Because the mass density vanishes at the upper surface, so too does the mass flux.

The stream function for the fundamental mode $n = 0$ (Figures 9(a), (b)) should be compared to the results of the numerical simulation illustrated in Figure 1(b). Here and in the anelastic simulations shown in Figure 1, the vertical elongation of the vortical columns is a function of the density stratification. The most obvious difference between the eigenfunctions derived here and in the numerical simulation is the cellular tilt. The numerical simulations demonstrate that the upper portion of each cell is centered at a higher longitude than the lower portion. Such tilting behavior—or in extreme cases, spiraling behavior—is a common feature that appears in diffusive solutions in spherical

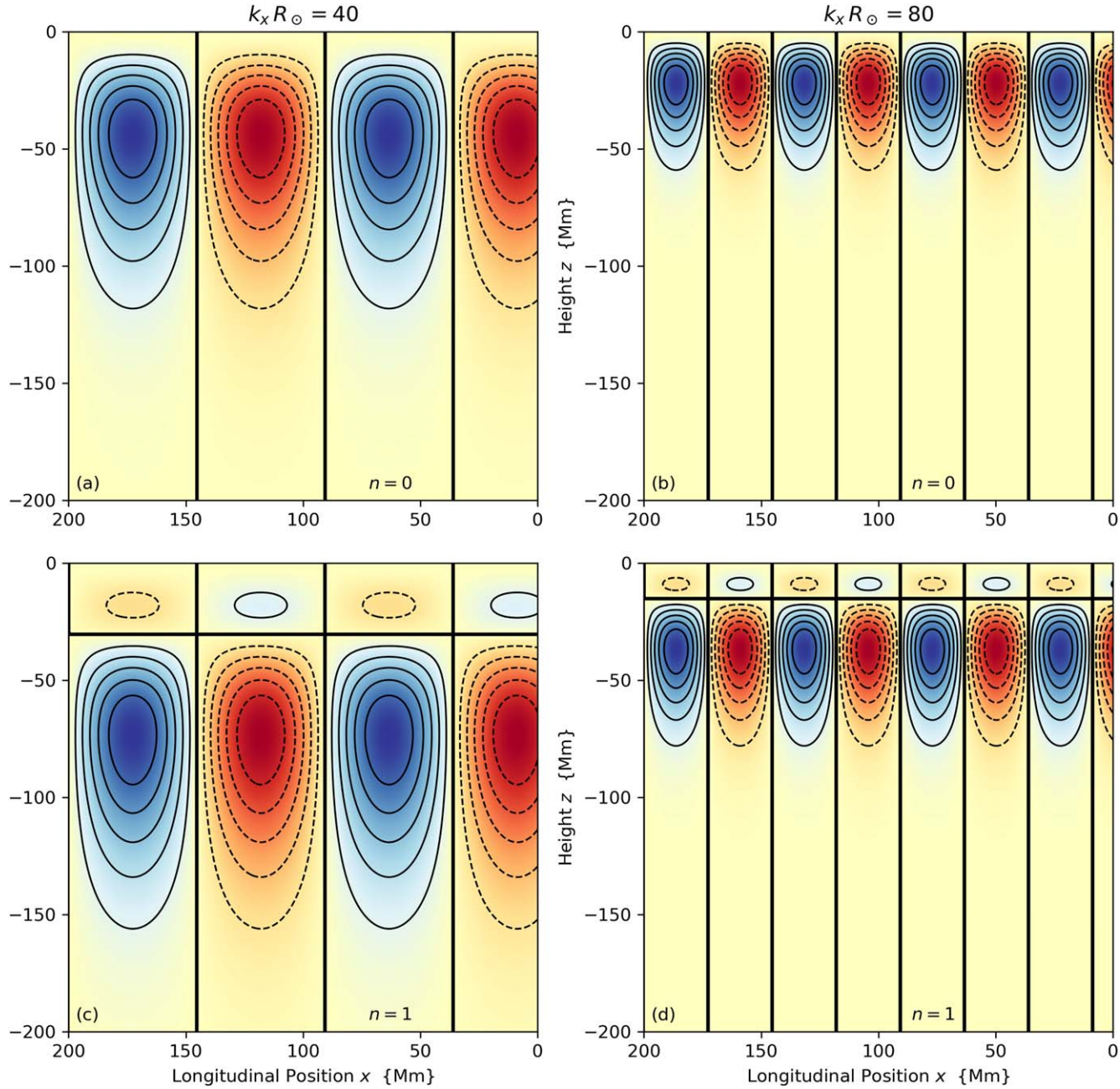

Figure 9. The stream function for the mass flux for four eigenmodes within a semi-infinite polytropic atmosphere. Red tones with dashed black isocontours indicate negative values of the stream function, and blue tones and solid isocontours positive values. The flow field is being viewed on a section of the equatorial plane as viewed from above the north pole. Motion in this plane is clockwise (anticyclonic) along the isocontours when the stream function is negative, and counterclockwise (cyclonic) along the contours for positive values. The upper row of panels illustrates the vortex structure for two fundamental radial modes $n = 0$ with different zonal wavenumbers, as indicated at the top of each panel. The lower panels correspond to the first radial overtone $n = 1$. The fundamental mode consists of single vortex or roll in radius, and two counterrotation rolls within a zonal wavelength. Each successive overtone stacks another roll in depth. The shapes of the rolls do not change as the zonal wavenumber increases. Instead, the spatial scale in all dimensions changes, maintaining the aspect ratio of the vortices.

geometry (Yano 1992; Zhang 1992; Jones et al. 2000, 2009). Neither of these effects are present in the calculations that we perform here.

5.4. Self-similarity of a Polytropic Atmosphere

In Section 4.3.1, we find that the eigenfrequencies for inertial oscillations within a semi-infinite isentropic atmosphere lack dependence on the zonal wavenumber. This unexpected result is due to the self-similarity of an infinitely deep polytropic atmosphere. All of the thermodynamic profiles (temperature, pressure, density, density scale height, etc.) are power-law functions of the depth and lack an imposed spatial scale. Hence, when trying to nondimensionalize the ODE that describes inertial waves within a polytropic atmosphere, the only length scale that is available is the zonal wavelength. There is only one way to form a nondimensional depth ζ (the independent variable of the governing equation), and it must be proportional to $-k_x z$. The resulting nondimensional form of the governing equation is thus self-similar, and so too are its

solutions. This is the reason that the eigenfunctions of the semi-infinite polytrope have the same shape, independent of the zonal wavenumber, but their spatial extent in all directions scales linearly with the zonal wavelength. For example, consider the eigensolutions illustrated in Figure 9; the shape of the rolls in the equatorial plane is independent of the longitudinal wavelength (compare the right and left panels). The only difference is their spatial scale. Waves with a short longitudinal wavelength have a short vertical wavelength, and vice versa.

The only way to break this self-similarity is by the imposition of a spatial scale through the boundary conditions. For a semi-infinite atmosphere, with boundary conditions placed at the origin and infinity, there is no imposed depth. Hence, the boundary conditions are also self-similar and the resulting eigenfrequencies can only depend on the stratification (through the polytropic index) and on the rotation rate. However, when boundaries are placed at finite depths within the polytropic atmosphere, the depth of the domain provides a length scale and the eigenfunctions and eigenfrequencies can now depend on the wavenumber. For example, if we place boundaries at the origin and at a depth of $z = -D$, as we did in Section 4.3.2, the eigenfrequencies can now depend on the zonal wavenumber through the combination $k_x D$.

5.5. The f Mode

From Equations (15) and (16), one can deduce that there is a solution that is incompressible and has vanishing Lagrangian pressure fluctuation everywhere $\delta\varpi = 0$. In order to avoid the trivial solution, the dispersion relation must satisfy $\omega^4 = \sigma^4$. The negative root, $\omega^2 = -\sigma^2$, corresponds to an unphysical solution with an unbounded energy density. The positive root, $\omega^2 = \sigma^2$, leads to the traditional f mode, or surface gravity wave, that has the same exponential behavior as the f mode for a nonrotating star, but a modified eigenfrequency:

$$w = -iu = \exp(k_x z)\, e^{ik_x x}\, e^{-i\omega t}, \tag{74}$$

$$\omega = \pm(gk + \Omega^2)^{1/2} - \Omega. \tag{75}$$

This dispersion relation is rather different from that of Poincaré waves because in our model the gravitational acceleration and the rotation vector are orthogonal, while in the traditional derivation of Poincaré waves the two vectors are parallel.

In the limit of slow rotation, we recover the traditional dispersion relation for deep water waves, but with a rotational correction:

$$\omega = \pm\sqrt{gk} - \Omega + \cdots. \tag{76}$$

However, for rapid rotation, there is a fast retrograde solution that is primarily an inertial oscillation,

$$\omega = -2\Omega - \frac{gk}{2\Omega} + \cdots, \tag{77}$$

and a slow prograde solution that is a mode of strongly mixed character,

$$\omega = \frac{gk}{2\Omega} + \cdots. \tag{78}$$

Figure 3 presents the frequency of both the prograde and retrograde surface gravity waves using the dotted–dashed green curves. When the rotation is strong, the anisotropy between the prograde and retrograde solutions can be rather extreme. In the right panel (rapid rotation), the prograde f mode's frequency is nearly equal to the upper frequency bound for the gravito-inertial waves, while the retrograde f modes shadows the boundary of the retrograde acoustic waves.

5.6. Observability of Thermal Rossby Waves in the Sun's Convection Zone

Recent observations of inertial oscillations in the Sun have been of three types: classical equatorially confined Rossby waves (Löptien et al. 2018; Alshehhi et al. 2019; Hanasoge & Mandal 2019; Liang et al. 2019; Hanson et al. 2020; Proxauf et al. 2020; Hathaway & Upton 2021), critical-latitude inertial modes (Gizon et al. 2020, 2021), and high-latitude inertial modes (Bogart et al. 2015; Gizon et al. 2021; Hathaway & Upton 2021). Thermal Rossby waves have not yet been observed. Why is this, when thermal Rossby waves are such a prominent feature in laboratory experiments and in numerical simulations of the solar convection zone?

We suggest two related possibilities: the thermal Rossby waves are all unstable, or the potentially stable long-wavelength waves have a cavity that is too deep to easily measure the waves at the solar surface. Convection in a star like the Sun, and in fact all stars, is highly supercritical. Thus, the thermal Rossby waves that appear at convective onset are not those that we should expect to see in solar observations. Instead, due to the extreme level of turbulence, we should expect to see the highly nonlinear cousins of those thermal Rossby waves that appear under more laminar conditions. Surprisingly, numerical simulations suggest that the spatial scale of the most unstable thermal Rossby wave persists in highly turbulent regimes (Hindman et al. 2020a). This spatial scale is often associated with what are termed convective banana cells (e.g., Wilson 1988; Miesch et al. 2000; Hotta et al. 2015; Nelson et al. 2018). Despite the fact that banana cells are immediately obvious to the eye in movie sequences from convection simulations, they do not form an obvious feature in spectra when the fluid is sufficiently turbulent (e.g., Hindman et al. 2020a). The power from these nonlinear waves is broadly spread across azimuthal order m, harmonic degree ℓ, and temporal frequency ω. Thus, the power does not form a clean dispersion relation that would verify its wavelike nature. One can deduce that the convective features propagate prograde relative to the differential rotation, but extracting more information has proved problematic.

Further, we must admit that it is uncertain what spatial scale should typify thermal Rossby waves in the Sun. The convective columns that appear in numerical simulations possess zonal wavenumbers that depend on the convection's Rossby number Ro (Featherstone & Hindman 2016). Unfortunately, the Sun's Rossby number is not well-constrained observationally. Thus, we are biased by those numerical models that produce dynamos with desirable properties. For example, global-scale dynamo simulations with low Rossby numbers, on the order $\mathrm{Ro} \sim 10^{-2}$, can generate cycling dynamo solutions (e.g., Ghizaru et al. 2010; Brown et al. 2011; Racine et al. 2011; Käpylä et al. 2012; Fan & Fang 2014) with equatorward migration of magnetic field (e.g., Käpylä et al. 2013). When the Rossby number has such a low value, the spatial scale associated with the thermal Rossby waves is typically rather small, corresponding to an azimuthal order of $m \sim 100$ (Featherstone & Hindman 2016). Unfortunately, in actual solar observations,

such short-wavelength waves would be easily confused with and masked by supergranulation.

All of these difficulties have so far made the search for peaks in the power spectra of the observed velocity field an unfruitful method to detect thermal Rossby waves. Instead, identifying thermal Rossby waves may require careful long-duration averages of the correlations between flow components that are indicative of the thermal Rossby wave's horizontal wave function. Such correlations may have already been detected years ago by Schou (2003) and Gizon et al. (2003) when they found wavelike properties in the supergranulation signal.

Even if the conjecture that we proposed in Section 5.1 is correct, and the lower half of the convection zone can indeed form a waveguide for long-wavelength thermal Rossby waves, those wave modes may not be visible at the surface. Assessing the visibility of the gravito-inertial modes would require knowing how the waves are excited and damped, thus allowing estimates of the mode amplitude to be made. Further, since the cavity is confined to the deeper layers of the convection zone, the wave function at the surface (where it can be measured) will have undergone many e-folding decay lengths. A similar problem exists for the Sun's g modes. The stellar physics community is certain that gravity modes must exist in the Sun's radiative interior, but we have not convincingly detected the action of such modes at the solar surface.

The very sensitivity of the thermal Rossby waves to the superadiabatic gradient, which leads to all of the nuisances in the observability of those modes, would make the thermal Rossby waves, if detected, an excellent seismic diagnostic of the superadiabaticity in the convection zone. Because the thermal Rossby waves tend to be confined near the equator (see Figure 1), they would be most sensitive to the gradient at low latitudes. It might be possible to assess weak latitudinal variations in the buoyancy frequency if the information from thermal Rossby waves were to be combined with observations of the high-latitude inertial oscillations that were recently discovered by Gizon et al. (2021). As discussed in Gizon et al. (2021), the high-latitude modes also possess sensitivity to the superadiabaticity, but in the polar regions.

We would like to thank Jon Aurnou, Maria Camisassa, Keith Julien, and Lydia Korre for useful discussions and for providing early feedback that influenced the development of this manuscript. This work was supported by NASA through grants 80NSSC17K0008, 80NSSC18K1125, 80NSSC19K0267, and 80NSSC20K0193. R.J. would like to acknowledge the support of MSRC (SoMaS), University of Sheffield (UK), and is grateful to the Science and Technology Facilities Council (STFC) grant ST/V000977/1.

ORCID iDs

Bradley W. Hindman https://orcid.org/0000-0001-7612-6628
Rekha Jain https://orcid.org/0000-0002-0080-5445

References

Abramowitz, M., & Stegun, I. 1964, Handbook of Mathematical Functions (New York: Dover), 505
Alshehhi, R., Hanson, C. S., Gizon, L., & Hanasoge, S. 2019, A&A, 622, 124
Ando, H. 1989, PASJ, 41, 289
Azouni, M. A., Bolton, E. W., & Busse, F. H. 1985, GApFD, 34, 301
Bekki, Y., Cameron, R. H., & Gizon, L. 2022, A&A, 662, A16
Bogart, R. S., Baldner, C. S., & Basu, S. 2015, ApJ, 807, 125
Brown, B. P., Browning, M. K., Brun, A. S., Miesch, M. S., & Toomre, J. 2011, ApJ, 731, 69
Brown, B. P., Vasil, G. M., & Zweibel, E. G. 2012, ApJ, 756, 109
Bryan, G. H. 1889, RSPTA, 180, 187
Busse, F. H. 1970, JFM, 44, 441
Busse, F. H. 2002, PhFl, 14, 1301
Busse, F. H., & Hood, L. L. 1982, GApFD, 21, 59
Busse, F. H., & Simitev, R. D. 2014, JFM, 751, 216
Busse, F. H., Zhang, K., & Liao, X. 2005, ApJL, 631, L171
Cai, T., Yu, C., & Wei, X. 2021, ApJ, 914, 11
Chamberlain, J. A., & Carrigan, C. R. 1986, GApFD, 35, 303
Christensen-Dalsgaard, J. 2003, Lecture Notes on Stellar Oscillations (5th ed.; Grundforskningsfond: Aarhus Universitet), 75
Christensen-Dalsgaard, J., Dappen, W., Ajukov, S. V., et al. 1996, Sci, 272, 1286
Cordero, S., & Busse, F. H. 1992, GeoRL, 19, 733
Damiani, C., Cameron, R. H., Birch, A. C., & Gizon, L. 2020, A&A, 637, A65
Dormy, E., Soward, A. M., Jones, C. A., Jault, D., & Cardin, P. 2004, JFM, 501, 43
Fan, Y., & Fang, F. 2014, ApJ, 789, 35
Featherstone, N. A., Edelmann, P. V. F., Gassmoeller, R., et al. 2021, geodynamics/Rayleigh: Rayleigh v1.0.1, Zenodo, doi:10.5281/zenodo.5774039
Featherstone, N. A., & Hindman, B. W. 2016, ApJ, 818, 32
Ghizaru, M., Charbonneau, P., & Smolarkiewicz, P. 2010, ApJL, 715, L133
Gibbons, M. P. 1980, JFM, 96, 493
Gizon, L., Cameron, R. H., Bekki, Y., et al. 2021, A&A, 652, L6
Gizon, L., Duvall, T. L., Jr., & Schou, J. 2003, Natur, 421, 43
Gizon, L., Fournier, D., & Albekioni, M. 2020, A&A, 642, A178
Glatzmaier, G. A., & Gilman, P. A. 1981, ApJS, 45, 381
Gough, D. O. 1993, in Les Houches Session XLVII, Astrophysical Fluid Dynamics, ed. J.-P. Zahn & J. Zinn-Justin (Amsterdam: Elsevier), 399
Greenspan, H. 1968, The Theory of Rotating Fluids (London: Cambridge Univ. Press)
Hanasoge, S., & Mandal, K. 2019, ApJL, 871, L32
Hanson, C. S., Gizon, L., & Liang, Z.-C. 2020, A&A, 635, 109
Hathaway, D. H., & Upton, L. A. 2021, ApJ, 908, 160
Hide, R. 1966, RSPTA, 259, 615
Hindman, B. W., Featherstone, N. A., & Julien, K. 2020a, ApJ, 898, 120
Hindman, B. W., Featherstone, N. A., & Julien, K. 2020b, Morphological Classification of the Convective Regimes in Rotating Stars, doi:10.17605/osf.io/qbt32
Hindman, B. W., & Zweibel, E. G. 1994, ApJ, 436, 929
Hotta, H., Rempel, M., & Yokoyama, T. 2015, ApJ, 798, 51
Jones, C. A., Kuzanyan, K. M., & Mitchell, R. H. 2009, JFM, 634, 291
Jones, C. A., Soward, A. M., & Mussa, A. I. 2000, JFM, 405, 157
Kaplan, E. J., Schaeffer, N., Vidal, J., & Cardin, P. 2017, PhRvL, 119, 094501
Käpylä, P. J., Mantere, M. J., & Brandenburg, A. 2012, ApJL, 755, L22
Käpylä, P. J., Mantere, M. J., Cole, E., Warnecke, J., & Brandenburg, A. 2013, ApJ, 778, 41
Lamb, H. 1945, Hydrodynamics (New York: Dover), 541
Lanza, A. F., Gizon, L., Zaqarashvili, T. V., Liang, Z.-C., & Rodenbeck, K. 2019, A&A, 623, A50
Lee, U., & Saio, H. 1986, MNRAS, 221, 365
Lee, U., & Saio, H. 1987, MNRAS, 224, 513
Lee, U., Strohmayer, T. E., & van Horn, H. M. 1992, ApJ, 397, 674
Li, G., Van Reeth, T., Bedding, T. R., Murphy, S. J., & Antoci, V. 2019, MNRAS, 487, 782
Liang, Z.-C., Gizon, L., Birch, A. C., & Duvall, T. L., Jr. 2019, A&A, 626, A3
Lindblom, L., & Ipser, J. R. 1999, PhRvD, 59, 044009
Lockitch, K. H., & Friedman, J. L. 1999, ApJ, 521, 764
Löptien, B., Gizon, L., Birch, A. C., et al. 2018, NatAs, 2, 568
Mandal, K., Hanasoge, S., & Gizon, L. 2021, A&A, 652, 96
Mason, P. J. 1975, RSPTA, 278, 397
Matsui, H., Heien, E., Aubert, J., et al. 2016, GGG, 17, 1586
Miesch, M. S., Elliott, J. R., Toomre, J., et al. 2000, ApJ, 532, 593
Nelson, N. J., Featherstone, N. A., Miesch, M. S., & Toomre, J. 2018, ApJ, 859, 117
Osaki, Y. 1974, ApJ, 189, 469
Ouazzani, R.-M., Ligniéres, F., Dupret, M.-A., et al. 2020, A&A, 640, A49
Papaloizou, J., & Pringle, J. E. 1978a, MNRAS, 182, 423

Papaloizou, J., & Pringle, J. E. 1978b, MNRAS, 195, 743
Provost, J., Berthomieu, G., & Rocca, A. 1981, A&A, 94, 126
Proxauf, B., Gizon, L., Löptien, B., et al. 2020, A&A, 634, A44
Racine, E., Charbonneau, P., Ghizaru, M., Bouchat, A., & Smolarkiewicz, P. 2011, ApJ, 735, 46
Rieutord, M. 1991, GApFD, 59, 185
Roberts, P. H. 1968, RSPTA, 263, 93
Saio, H. 1982, ApJ, 256, 717
Saio, H., Kurtz, D. W., Murphy, S. J., Antoci, V. L., & Lee, U. 2018, MNRAS, 474, 2774
Schou, J. 2003, ApJL, 596, L259
Smith, C. A., Speer, K. G., & Griffiths, R. W. 2014, JPO, 44, 2273
Sommeria, J., Meyers, S. D., & Swinney, H. L. 1991, in Nonlinear Topics in Ocean Physics, ed. A. R. Osborne (North Holland: Elsevier), 227
Soward, A. M., & Jones, C. A. 1983, QJMAM, 36, 19
Unno, W., Oskai, Y., Ando, H., Saio, H., & Shibahashi, H. 1989, Nonradial Oscillations of Stars (2nd ed.; Tokyo: Univ. Tokyo Press), 309
Van Reeth, T., Mombarg, J. S. G., Mathis, S., et al. 2018, A&A, 618, A24
Wilson, P. R. 1988, SoPh, 117, 217
Wolff, C. L., & Blizard, J. B. 1986, SoPh, 105, 1
Wu, Y. 2005, ApJ, 635, 674
Yano, J. I. 1992, JFM, 243, 103
Zaqarashvili, T. V., Albekioni, M., Ballester, J. L., et al. 2021, SSRv, 217, 15
Zhang, K. 1992, JFM, 236, 535